International Journal of Impact Engineering 173 (2023) 104437

Contents lists available at ScienceDirect

International Journal of Impact Engineering

journal homepage: www.elsevier.com/locate/ijimpeng

Performance of thin blast-loaded steel plates after ballistic impact from small-arms projectiles

Benjamin Stavnar Elveli *, Torodd Berstad, Tore Børvik, Vegard Aune

Structural Impact Laboratory (SIMLab), Department of Structural Engineering, NTNU – Norwegian University of Science and Technology, NO-7491 Trondheim, Norway
Centre for Advanced Structural Analysis (CASA), NTNU, NO-7491 Trondheim, Norway

ARTICLE INFO

Keywords:
Strength-ductility trade-off
Ballistic impact
Shock tube
Combined impact and blast loading

ABSTRACT

It is known from real blast-load events that the combined effect of fragment impact and blast loading is more severe than the effect of the blast loading alone. The present study investigates this effect by comparing the blast response of thin steel plates pre-damaged by either ballistic impacts or idealized pre-cut circular holes under similar blast loading conditions. The ballistic impacts were performed with a rifle, firing 7.62 mm APM2 projectiles, and the subsequent blast loading was applied in a shock tube facility. During the blast tests, pressure measurements and two high-speed cameras were used to record the dynamic response of the target plates and allowed for a reliable experimental procedure. To investigate the strength-ductility trade-off dilemma of the material during extreme loading, three different steels with different levels of strength and ductility were used in the tests. Numerical simulations were conducted in an attempt to obtain more insight into the fracture characteristics of the plates.

For similar loading conditions and material, the target plates exposed to ballistic impact showed a reduced resistance to fracture during blast loading compared with target plates containing pre-formed circular holes. As for the effect of material strength and ductility, the global deformation decreased, while the localization of plasticity increased, with an increased material strength. The fracture resistance was also observed to decrease with increased material strength. The numerical models were able to capture the main trends observed in the physical tests, i.e., a decrease in fracture resistance with initial ballistic impact, and a reduction in fracture resistance with increased material strength. The numerically predicted crack paths also showed a strong dependence upon the initial cracks caused by the petals from the ballistic impacts.

1. Introduction

Blast waves can be caused by industrial accidents, military actions or terrorist attacks, subjecting surrounding structures to extreme loading. In addition, the blast wave can accelerate objects in its proximity to high velocities. These objects are typically categorized as primary and secondary fragments. Primary fragments are defined as objects initially contained in the explosive device (e.g., ball bearings [1]) or parts from the fractured casing of the explosive (e.g., a shell or a vehicle). Fragments may impact the structure before, during or after the arrival of the blast wave, depending on the distance between the explosive charge and the structure [2]. These fragments may perforate the structure, introducing both geometrical defects and initial material damage. A fragment perforation prior to the arrival of the blast wave, may reduce the load-carrying capacity of the structure and the combined effects of blast and fragment impact can be more severe than the blast loading acting alone (see e.g. [3–7]). However, the literature is rather scarce when it comes to studies on the combined effects of blast and fragment loading, and most of the existing research on combined loading effects are on concrete structures [8–12]. Nevertheless, modern civilian structures tend to be more lightweight and flexible than the traditional fortified structures, and the responses of thin-walled metallic plates have received increased interest over the last few years [13–15].

Pre-cut defects may imitate the geometrical defects imposed by fragment impact. It was shown in [16] that idealized perforations reduce the plates resistance both against plastic deformations and fracture. Pre-cut defects typically introduce sharp corners and local areas of increased stress, which amplifies ductile crack initiation and growth. In [17–19], the blast response of target plates containing pre-formed circular holes and pre-formed square holes was compared. All three

* Corresponding author.
E-mail address: benjamin.s.elveli@ntnu.no (B.S. Elveli).

https://doi.org/10.1016/j.ijimpeng.2022.104437
Received 13 June 2022; Received in revised form 21 October 2022; Accepted 10 November 2022
Available online 21 November 2022

studies concluded that the fracture resistance during blast loading was dependent upon the pre-formed hole geometry, where the square perforations resulted in the lowest resistance. Further, Granum et al. [20] found that the effect of the number, distribution and orientation of pre-cut slits in thin blast-loaded aluminium plates strongly affects both the fracture resistance and the failure mode. However, during a fragment perforation, the corresponding fragment hole depend upon the size and shape of the fragment. Moreover, additional material damage can occur in the proximity of the hole. These effects are not covered by studies on plates with idealized preformed defects, which could lead to non-conservative estimates of the fracture resistance during blast loading.

Experimental studies on the combined effect of fragment and blast loading are ideal as they represent the actual physics of the problem, whereas theoretical and numerical methods need to be validated against experimental data to ensure that they provide reliable predictions. Testing on full-scale prototype structures is normally considered too expensive, time-consuming, and infeasible, and is seldom an option. Therefore, controlled small-scale experiments on simple structures have a significant potential in improving our understanding of the combined effect of blast loading and fragment impact. Cai et al. [21] performed an experimental study on multi-layered aluminium foam sandwich panels, exposed to a combined loading from TNT and 52 attached prefabricated square fragments. The experimental results gave three different responses for the backplate of the sandwich panel; petaling, cracking, or only deformation. Li et al. [22] applied a similar setup for an experimental and numerical study on composite laminates subjected to blast and fragment loading. It was concluded that the applied numerical model gave reliable results, and was in good agreement with the experiments.

From a numerical point of view, fragment impact on a structure is similar to ballistic impact problems. A well known challenge in numerical modelling of ballistic impact is that a very fine discretization of the structure is required to obtain reliable predictions (see e.g., [23,24]). Also, high-velocity impacts are commonly governed by local deformations in the material with a relatively short duration. In contrast, the deformation of blast loaded thin-walled structures is normally governed by global deformation, with a significantly longer duration [16,25,26]. For a blast simulation to run within a reasonable computational (CPU) time, a much coarser discretization of the deforming structure is required. This is challenging when modelling the combined effect of fragment impact and blast loading of plated structures, especially if a realistic fracture mode from the fragment impact phase and a feasible CPU cost during the blast loading phase of the simulation are important.

In previous studies, fragment impact prior to blast loading has been represented by pre-cut defects with idealized geometries. This study aims to investigate the effect of more realistic perforations on the blast resistance of thin steel plates, assuming that the fragment impacts before the blast wave. First, the plates were perforated by 7.62 mm APM2 projectiles in a ballistic range. Then, the perforated plates were subjected to blast loading in a shock tube facility. Three different steel qualities were applied for the target plates to also include the strength-ductility trade-off [27]. Finally, numerical simulations were conducted to gain more insight into the fracture characteristics of the blast-loaded plates. The main objectives of this study are: (1) to provide new insight into the effect of realistic fracture modes on the blast resistance of thin steel plates, comparing the performance of plates with ballistic perforations to that of plates with idealized pre-cut circular holes under similar blast loading conditions; (2) address challenges in the numerical modelling and simulation of combined ballistic impact and blast loading; and (3) evaluate the capability of current computational methods in predicting the dynamic response and fracture resistance of the materials under consideration.

2. Materials

To study the effect of strength and ductility on the fracture resistance during testing, three different steel qualities were used, i.e., Docol 600DL, Docol 1000DP and Docol 1400M. All target plates were produced by SSAB [28] and cold rolled to a thickness of 0.8 mm. Docol 600DL represents a dual-phase, medium strength, high-hardening steel with good formability compared to its strength. It has a reported yield strength in the range of 280–360 MPa and an ultimate tensile strength of 600–700 MPa. Docol 1000DP is also a dual-phase steel, but with a higher martensite fraction than Docol 600DL. Docol 1400M is a strong martensitic steel with a reported minimum yield strength of 1150 MPa and an ultimate tensile strength in the range of 1400–1600 MPa. The high strength is obtained by a rapid water quenching of an austenitic steel so that the carbon atoms are unable to diffuse and form cementite. The chemical compositions for all three materials are given in Table 1. For simplicity, the following abbreviations have been introduced for the material names; Docol 600DL is denoted D6, Docol 1000DP is denoted D10, and Docol 1400M is denoted D14.

2.1. Material testing

Quasi-static uniaxial tension tests were carried out for all three materials in an Instron 5982 testing machine at a constant deformation rate of 2.1 mm/min. The specimen geometry is given in Fig. 1(a). With a gauge length of 70 mm, the applied deformation rate corresponds to a global strain rate of $\dot{\epsilon}_0 = 5 \cdot 10^{-4}$ s^{-1}. The specimens were cut from the 0.8 mm sheets with 0°, 45° and 90° relative to the rolling direction. Three repetitions were performed in each direction for each material to reveal possible anisotropy.

To determine the engineering stress–strain curves in Fig. 1(b), the force was measured by the load cell in the testing machine and the displacement was obtained from 2D-DIC using a virtual extensometer. During each test, the force measurements were synchronized with images of the test specimen at a sampling rate of 4 Hz. Prior to the tests, each specimen was spray-painted with a black and white speckle pattern, allowing for two-dimensional (2D) digital image correlation (DIC). A virtual extensometer of 60 mm was applied to calculate the engineering strain. The engineering stress was calculated by scaling the force with the initial gauge area of the test specimen, measured with a digital calliper.

Fig. 1(b) confirms the step-wise change in yield stress, strength, and strain to fracture for the three materials under consideration. That is, the yield stress, strength and strain to fracture for Docol 1000DP lies between Docol 600DL and Docol 1400M. For all three materials, some variations are seen in the engineering failure strain. However, the variation between tests in the three different directions is of a similar magnitude as the variation between repeated tests within each direction. For both the flow and yield stress, no significant variation was observed. Gruben et al. [29] investigated both the D6 and D14 materials with similar results for the uniaxial tension tests, and concluded that the plastic anisotropy was negligible. This was later confirmed by Aune et al. [26].

3. Component tests

The main objective of the component tests was to study the effect of ballistic perforations on the subsequent blast response of thin steel plates, and to compare the performance of these plates to that of plates with idealized holes under similar blast loading conditions. Hence, plates with pre-cut circular holes with a diameter similar to the projectile were also tested against blast loading to establish a reference to the ballistic impact hole containing damage and petalling cracks. The target plates were first subjected to ballistic impact, before exposed to blast-like loading using two different load intensities for each plate configuration.

Table 1
Chemical composition of the three materials (in wt.%) taken from the data sheet of the current batch.

Material	C	Si	Mn	P	S	Cr	Ni	V	Cu	Al	Nb+Ti	B	N
D6	0.095	0.30	1.45	0.012	0.003	0.02	0.03	0.01	0.01	0.052	0.0	0.0003	0.003
D10	0.137	0.20	1.51	0.008	0.003	0.02	0.04	0.01	0.01	0.04	0.015	0.0002	0.007
D14	0.173	0.19	1.32	0.011	0.003	0.03	0.04	0.02	0.15	0.042	0.03	0.0017	0.004

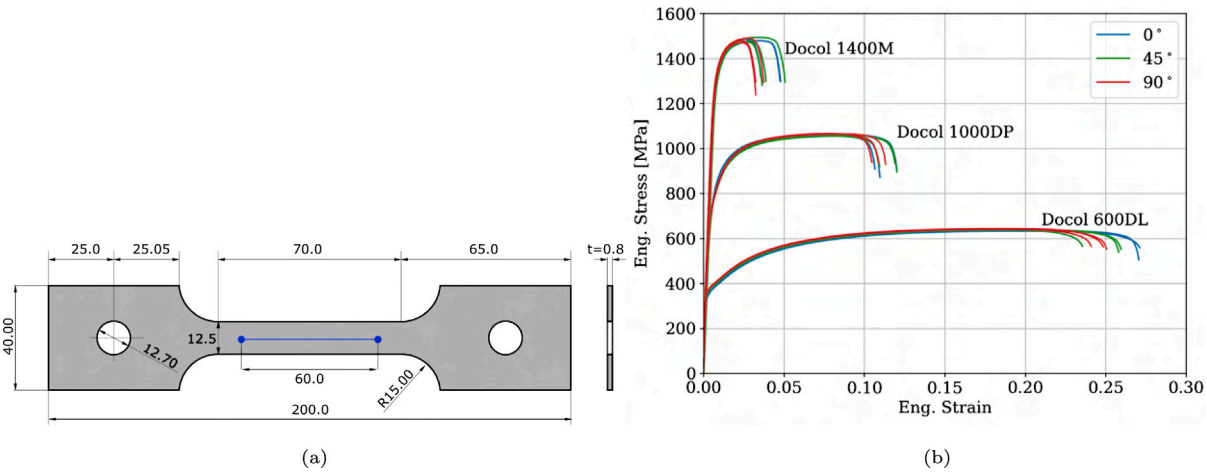

Fig. 1. (a) Sketch of the uniaxial tension test specimen and the position of the virtual extensometer marked with a blue line, and (b) the corresponding engineering stress–strain curves for all three materials. All dimensions are in mm. (For interpretation of the references to colour in this figure legend, the reader is referred to the web version of this article.)

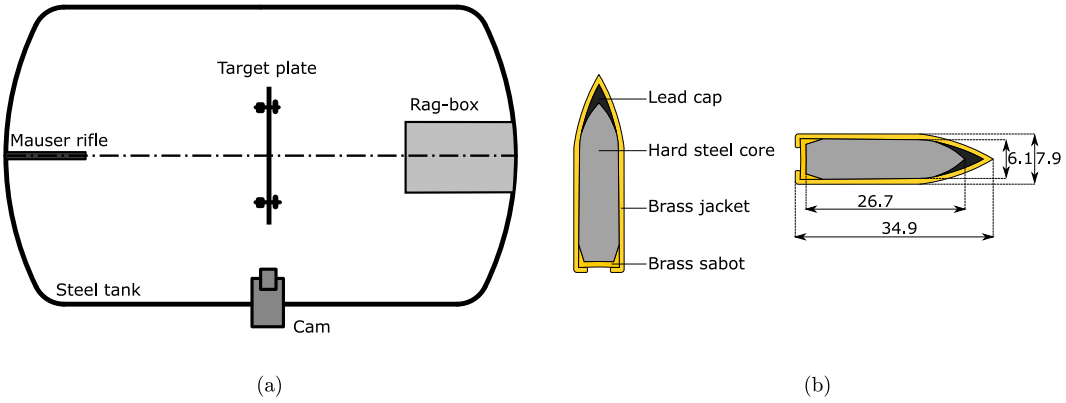

Fig. 2. The experimental setup during the ballistic impact tests: (a) the target plate and smooth bore Mauser rifle inside the steel tank, and (b) the material composition and dimensions of the 7.62 APM2 bullet. All dimensions are in mm.

3.1. Ballistic impact tests — setup

The ballistic tests were done in the gas gun facility at SIMLab [30]. Instead of firing the projectiles from the gas gun itself, a smooth bore Mauser rifle was mounted inside the steel tank of the gas gun as illustrated in Fig. 2(a). 7.62 mm APM2 projectiles were used as projectiles, with the dimensions and composition given in Fig. 2(b). One shot was fired against the centre of each target plate, with two repetitions for each of the three materials. This leaves a total of 6 ballistic impact tests.

The dimensions of the target plates and position of the pre-cut circular and ballistic impact holes are illustrated in Fig. 3. The intention of the ballistic perforations at the same position and with similar hole diameters as the pre-cut circular holes, was to investigate the effect of damage and petalling cracks from ballistic impacts on the blast resistance of the plates. The initial velocities of the projectiles were chosen to be significantly higher than the ballistic limit velocity, facilitating localized fracture modes limited to the point of impact. Hence, the ballistic limit velocity for these plates was not of interest in this study.

The penetration and perforation process of the target plates were recorded by a Phantom v2511 high-speed camera, and the pitch both before and after impact was confirmed to be low. The image series also allowed for accurate measurements of both the initial and residual velocities of the projectile, as well as observing the dynamic response of the plates and possible deformations of the projectiles. The initial and residual velocities were obtained by using a point-tracking algorithm on the high-speed images using the in-house DIC software eCorr [31].

3.2. Ballistic impact tests — results

The ballistic impact tests were conducted with initial projectile velocities in the range of 910 m/s–932 m/s, and the velocity reduction after perforation was less than 2% in all tests. Fig. 4(a) shows a representative image sequence of the ballistic impact event, where no visual damage or plastic deformation occurred in the projectiles. All target plates fractured by petalling, where three representative pictures of the exit holes are given in Fig. 4(b–d). Visual inspection of the target plates confirmed that the deformation was localized around the

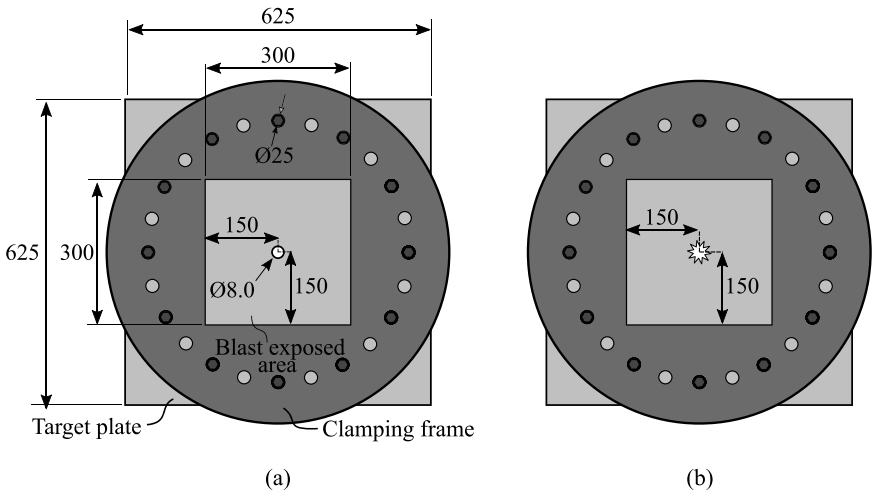

Fig. 3. The two plate geometries under consideration in this study: (a) The plate with pre-cut circular hole (C) geometry, and (b) the plate with the ballistic hole (B) geometry. All dimensions are in mm and the plates had a thickness of 0.8 mm.

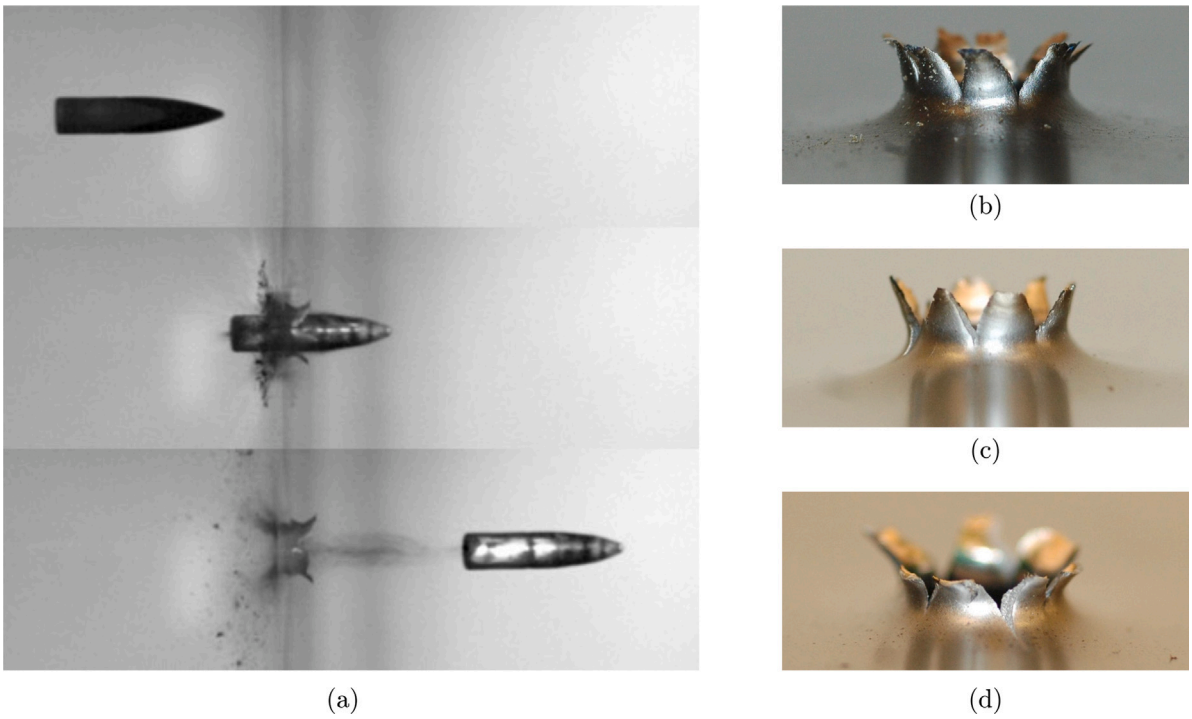

Fig. 4. Representative image sequence of the projectile perforation: (a) High-speed photography of the ballistic impact, and representative images of the corresponding fracture modes for (b) D6 plates, (c) D10 plates and (d) D14 plates.

impact hole. The measured diameters of the bullet holes were in the range 8.1 mm–8.4 mm, comparable to the plate geometry with pre-cut circular holes as shown in Fig. 3(a). It is noted that some of the petalling cracks extended slightly outside the periphery of the visual bullet hole (see e.g., Fig. 4(d)). However, no clear differences were observed in the petalling modes of the three materials, or between repeated tests. The important observation was that the ballistic impact tests succeeded in creating perforations containing local damage with good repeatability.

3.3. Blast load tests — setup

All blast load experiments were performed in the SIMLab Shock Tube Facility (SSTF). This test facility is thoroughly described and evaluated in terms of its performance to generate blast-like loading by Aune et al. [16,32], and is therefore only briefly presented in this section. The SSTF has proven to be an easily controllable alternative to explosive detonations and can be used to study the dynamic response of blast-loaded structures. A sketch of the SSTF is given in Fig. 5.

The propagation of the blast wave is initiated at the driver side of the shock tube and impacts the target plate just inside the steel tank at the right end of the tube. By keeping the length of the driver section short compared to the driven section, the resulting pressure waves will take on the characteristic form of a blast wave like that in a free-field air blast explosion [32,33]. In this study, all experiments were performed with a driver length of 0.77 m and compressed air was used to pressurize the driver section. A 16.20 m long low-pressure chamber denoted the driven section follows the driver section, and the test specimen is mounted at the right end of this section. The target plates were mounted to the shock tube by using a clamping assembly. The dimensions of the clamping assembly are given in Fig. 3.

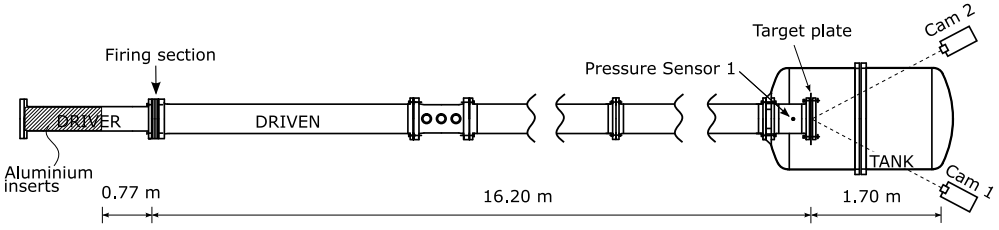

Fig. 5. Illustration of the SIMLab Shock Tube Facility (SSTF), where the pressure sensor used in this study (Sensor 1) is located 245 mm upstream the target plate [27].

Table 2
Experimental program.

Firing pressure	C	B
25 bar	D6_C_25 D10_C_25 D14_C_25	D6_B_25 D10_B_25 D14_B_25
35 bar	D6_C_35 D10_C_35 D14_C_35	D6_B_35 D10_B_35 D14_B_35

All target plates had dimensions of 625 mm × 625 mm × 0.8 mm and a blast-exposed area of 300 mm × 300 mm.

To monitor the tests, the facility is equipped with two high-speed cameras (Phantom v2511) and several pressure sensors (Kistler type 603B) for a synchronized sampling of data. The high-speed cameras operated at a frame rate of 37 kHz, while both the incoming and reflected overpressure were sampled with a frequency of 500 kHz at Sensor 1 in Fig. 5. Sensor 1 is located 245 mm upstream of the target plates and serves as the best available estimate for the pressure acting on the surface of the target plates. Hence, all pressure measurements presented in this study are measured at Sensor 1 and represent the overpressure relative to atmospheric conditions. After blast loading, the plates were measured in-situ with a portable Romer Absolute Arm 7525SI laser scanner that generates a point cloud of the deformed geometry of the tested plates.

Plates with pre-cut circular holes (C) and plates with ballistic holes (B) were tested against two different blast intensities for each material. For a complete comparison of all three materials and the effect of pre-cut circular holes versus ballistic holes, it was decided to apply the same two blast intensities for both geometries and all three materials. This leaves a total of 12 blast-load experiments. The complete test matrix for all blast tests is given in Table 2, where each test is named according to the convention DX_Y_Z. DX refers to the materials, i.e., either D6, D10 or D14. Y specifies the geometry of the plate, i.e., pre-cut circular hole (C) or ballistic hole (B). Z indicates the blast intensity labelled by the firing pressure in the driver section in bar. The firing pressures listed in Table 2 are rounded to the lower multiple of 5, i.e., 25 or 35.

3.4. Blast load tests — results

The presentation of the results focuses on the measured blast loading parameters from Sensor 1 (see Fig. 5), the global deformation fields of the target plates from the laser scans, and the crack initiation and propagation of cracks for a selection of representative tests. The firing pressure, the peak incoming pressure ($P_{so,max}$) and the peak reflected pressure ($P_{r,max}$), as well as the duration of the positive pressure phase (t_+) are all given in Table 3. The plate response under blast loading is also specified and divided into three response categories; no cracks, crack arrest, or total fracture.

Table 3
Blast parameters measured by Sensor 1 (Fig. 5). The firing pressure denotes the maximum pressure measured in the driver section right before rupture of the diaphragms. The peak incoming and peak reflected pressures at Sensor 1 are denoted $P_{so,max}$ and $P_{r,max}$, respectively. The duration of the positive phase of the reflected pressure at Sensor 1 is given by t_+.

Test	Firing pressure [bar]	$P_{so,max}$ [kPa]	$P_{r,max}$ [kPa]	t_+ [ms]	Plate response
D6_C_25	24.9	270.1	772.5	46.1	No cracks
D6_B_25	23.9	260.9	726.4	44.5	No cracks
D10_C_25	24.2	276.5	775.8	42.4	No cracks
D10_B_25	24.3	280.6	791.2	42.3	Crack arrest
D14_C_25	24.1	266.7	796.6	44.3	No cracks
D14_B_25	24.3	277.7	809.9	42.4	Crack arrest
D6_C_35	35.0	327.4	958.2	49.9	No cracks
D6_B_35	36.9	344.6	1020.2	45.9	Crack arrest
D10_C_35	36.7	343.6	1069.0	43.0	No cracks
D10_B_35	36.9	338.1	1019.6	45.0	Crack arrest
D14_C_35	37.0	344.1	1106.6	46.3	Crack arrest
D14_B_35	37.8	340.1	1053.5	–	Total fracture

This study does not aim to present a detailed evaluation of possible fluid–structure interaction (FSI) effects. The blast parameters are mainly presented to verify that the applied blast loads are similar and repeatable for each of the load intensities. As the reflected pressure may depend upon the deformation history of the blast loaded plates, this is done by comparing $P_{so,max}$ between repeated tests. For tests at the same blast intensity, minor variations are observed in $P_{so,max}$. It is also noted that $P_{r,max}$ seems to increase with increased material strength, which indicates that FSI effects depend on the material under consideration. Aune et al. [34] investigated the FSI effects during the dynamic response of blast-loaded thin steel plates. The target plates in that study were manufactured from the D6 material with a thickness of 0.8 mm. It was found that the peak pressure experienced a reduction between 4% and 15% depending on the blast intensity. However, FSI effects have not been investigated any further and are considered outside the scope of this study.

Fig. 6 presents the out-of-plane displacements of the plates as point clouds measured in-situ by the laser scanner after blast loading. The permanent displacements of the blast-exposed area are compared for all three plate materials when subjected to the lowest blast intensity. The colour map denotes the out-of-plane displacements with fringe levels given in the respective colour bars. For both geometries, the magnitude of the displacements decreases with an increase in material strength. As expected, the D6 plates experience the largest displacements, the D14 plates undergo the smallest displacements, whereas the D10 plates are positioned in-between the other two plate materials. It is also observed that the distribution of the deformations in the blast-exposed area changes with material. That is, the low strength material (D6) experiences the largest deformations and distributes the deformations over the largest area. As the material strength is increased, and the ductility decreased, the permanent deformations tend to localize in a smaller region at the plate centre. This is also in agreement with the findings of Refs. [20,27,35], because increased work hardening tends to distribute plasticity on a larger area of the plate. The global response within each plate material is however similar between the two hole

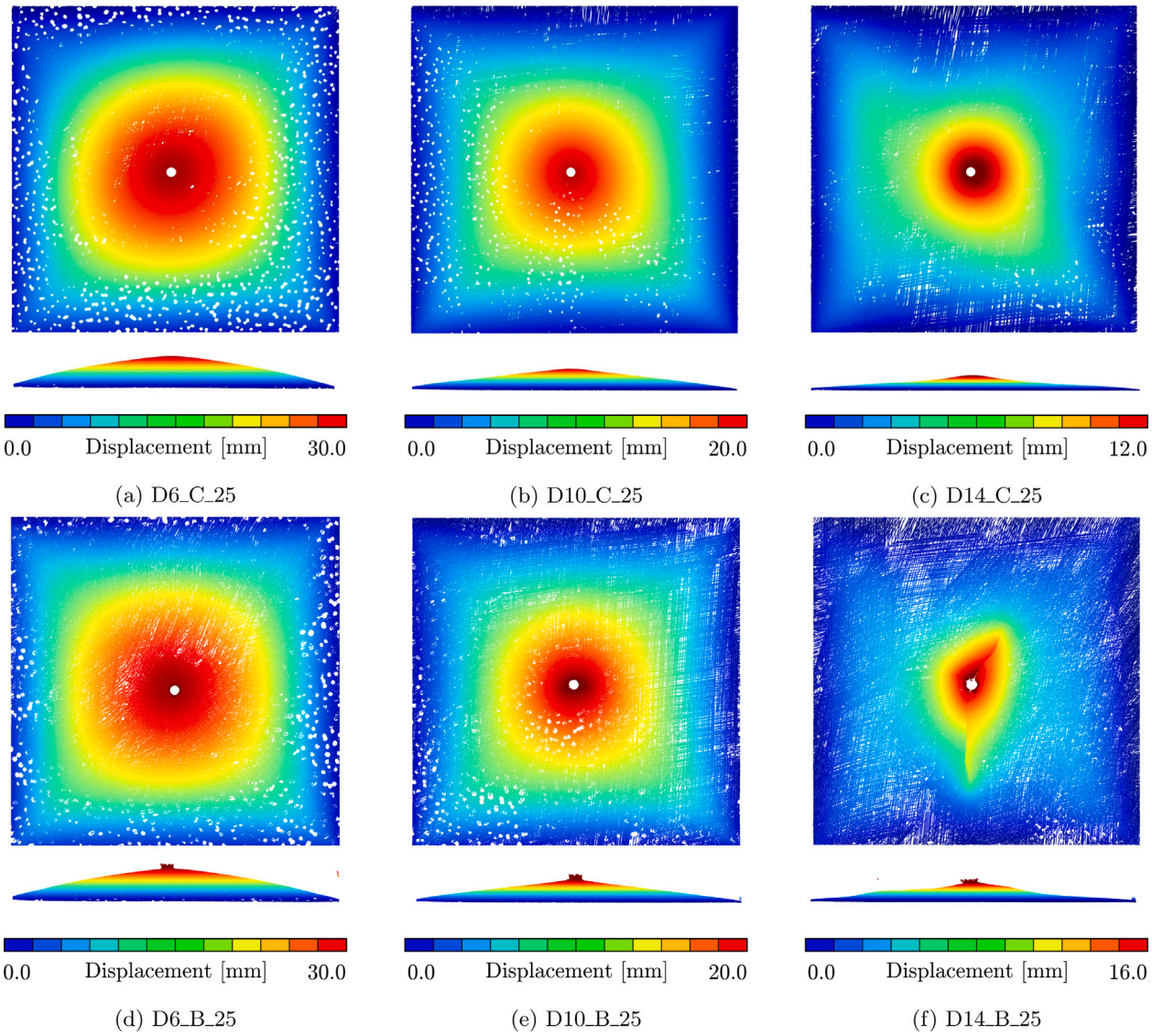

Fig. 6. Point clouds from the laser scans of the target plates after blast loading. The colour map indicates the out-of-plane displacements. The limits for each colour map is given in the respective test, and the test names are given in the subcaptions. Test D14_B_25 in (f) experienced fracture, which is the reason for the discontinuities in the displacement field. (For interpretation of the references to colour in this figure legend, the reader is referred to the web version of this article.)

geometries. It is noted that the D14_B_25 test (Fig. 6(f)) experienced significant cracking, and therefore increased displacements compared to the D14_C_25 test (Fig. 6(c)). The cracks are seen as discontinuities in the displacement field. Hence, provided that the plates do not fracture, the pre-damage does not seem to significantly affect the global deformations.

For the blast tests experiencing fracture, pictures showing the final state of the crack propagation are given for tests on D6 and D10 plates in Fig. 7, and for tests on D14 plates in Fig. 8. The arrested cracks in the D6 and D10 plates are rather short with crack lengths of about the same magnitude as the diameter of the ballistic impact hole. It is noted that both the number and length of the cracks are increased from D6_B_35 to D10_B_35, indicating that the D6 plate has greater resistance against both crack initiation and crack propagation than the D10 plate. The D14 plates resulted in two tests with arrested cracks and one test with total fracture (see Fig. 8). The arrested cracks in the D14 plates are significantly larger than the cracks for the D6 and D10 plates. Test D14_C_35 was the only test on the pre-cut circular hole (C) geometry experiencing arrested cracks and test D14_B_35 was the only test resulting in total fracture. This shows that the resistance against crack initiation and crack propagation is decreased when the material strength is increased, i.e., D6 plates have the highest resistance, D14 plates have the lowest, whereas D10 ends up in-between the other two. This confirms the results in Elveli et al. [27], where the strength-ductility trade-off was studied for thin steel plates with idealized, pre-cut defects. That is, plates with low material strength and high ductility resulted in better fracture resistance than stronger and less ductile plate materials.

Out of the 12 blast tests, 5 resulted in arrested cracks and one in total fracture. From Table 3, it is concluded that the plates with the ballistic holes (B) are more prone to fracture. This shows that the fracture resistance is reduced in the plates with ballistic holes, compared to the plates with idealized pre-cut circular holes. This trend was observed for all three materials. Both the locations of crack initiation and the directions of crack propagation during blast loading showed a strong dependence upon the petalling cracks resulting from the ballistic impact prior to the blast loading. From Figs. 7 and 8, it is seen that all arrested cracks in plates with the ballistic holes (B) were initiated at the initial petalling cracks. Thus, cracks started to propagate in the directions of the petals formed during the ballistic impact. It was interesting to note that the cracks propagated along other directions than the diagonals. The global response of thin, blast-loaded plates are

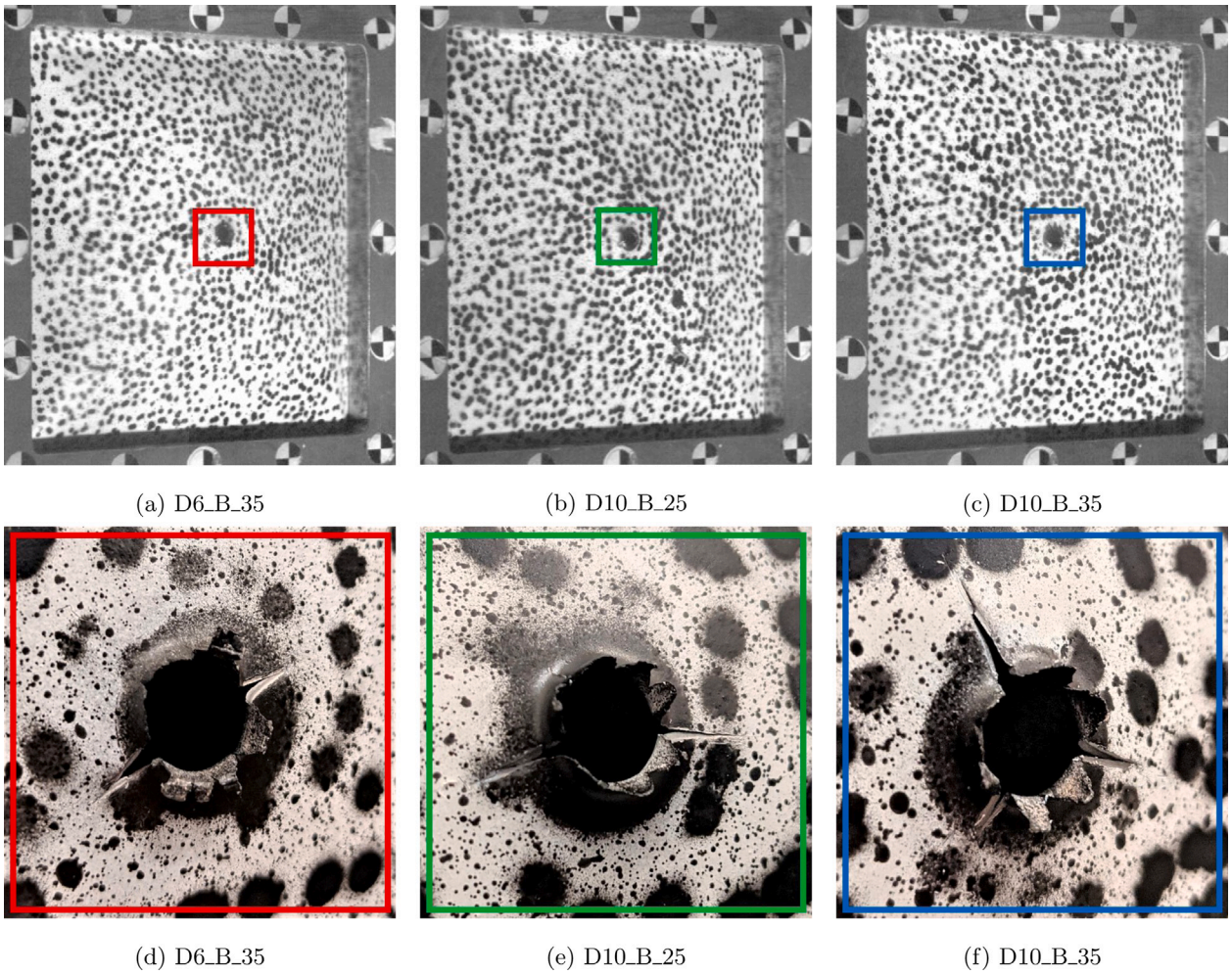

Fig. 7. Pictures of the final state after blast loading for all tests on D6 and D10 plates experiencing cracking. The full blast exposed area is shown in (a)–(c), and zoomed-in views of the arrested cracks are presented in (d)–(f).

typically characterized by plastic hinges travelling from the supports towards the centre of the plate, determining the deformed shape of the plate which is similar to a global dome. It is therefore often expected that the cracks will turn towards the diagonals on their way towards the plate boundary [36]. However, this was not the case in these tests. Test D14_B_35 showed that cracks propagated vertically and horizontally from the centre and all the way to the supports. It is also noted that, except for test D14_B_35, all crack initiations and propagations were unsymmetrical. This is contrary to the findings in previous studies on thin metallic plates with idealized pre-cut defects (see e.g., [16,20,27]), where cracks mainly initiated and propagated along the plate diagonals in a symmetrical manner.

4. Material modelling

4.1. Constitutive relation and failure criterion

The thermoviscoplastic constitutive relation applied in this study is based on a modified version of the Johnson–Cook model, and has proven to give good results for metallic materials under extreme loading conditions [16,20,37,38]. The flow stress accounts for plastic straining, elevated plastic strain rates, and temperature softening by

$$\sigma_{\text{eq}} = (A + R(p))\left(1 + \dot{p}^*\right)^c \left(1 - T^{*m}\right) \tag{1}$$

where A is the yield stress, $\dot{p}^*$ is the dimensionless plastic strain rate given by $\dot{p}^* = \dot{p}/\dot{p}_0$, where $\dot{p}$ is the current equivalent plastic strain rate and $\dot{p}_0 = 5.0 \times 10^{-4}$ s^{-1} is a reference strain rate. The strain rate sensitivity of the material is governed by c, while the temperature softening term is governed by the homologous temperature $T^* = (T - T_0)/(T_m - T_0)$, where T_0 and T_m describes a reference temperature and the melting temperature, respectively. The temperature softening exponent is given by m.

The equivalent flow stress σ_{eq} was determined by a Hershey yield surface, expressed in terms of the principal stresses $\sigma_i, i = 1, 2, 3$, as

$$\sigma_{\text{eq}} = \left(|\sigma_1 - \sigma_2|^a + |\sigma_2 - \sigma_3|^a + |\sigma_3 - \sigma_1|^a\right)^{\frac{1}{a}} \tag{2}$$

where the exponent a determines the shape of the yield surface. If $a = 2$ or $a = 4$, Eq. (2) describes a von Mises yield surface, while $a = 1$ or $a = \infty$ results in the Tresca yield criterion. Hence, for $a > 4$, the shape of the yield surface will lie between the von Mises and Tresca criteria. The work hardening $R(p)$ was described through a three-term Voce hardening law

$$R(p) = \sum_{k=1}^{3} Q_k \left(1 - e^{-c_k p}\right) \tag{3}$$

where Q_k and c_k are numerical parameters governing the saturation stress and hardening rate of the material, and p is the equivalent plastic strain. Lastly, material fracture was governed by element erosion and the Cockcroft–Latham (CL) ductile failure criterion [39], given by

$$D = \frac{W}{W_c} = \frac{1}{W_c}\int_0^p \langle\sigma_1\rangle dp, \qquad \langle\sigma_1\rangle = \max(\sigma_1, 0) \tag{4}$$

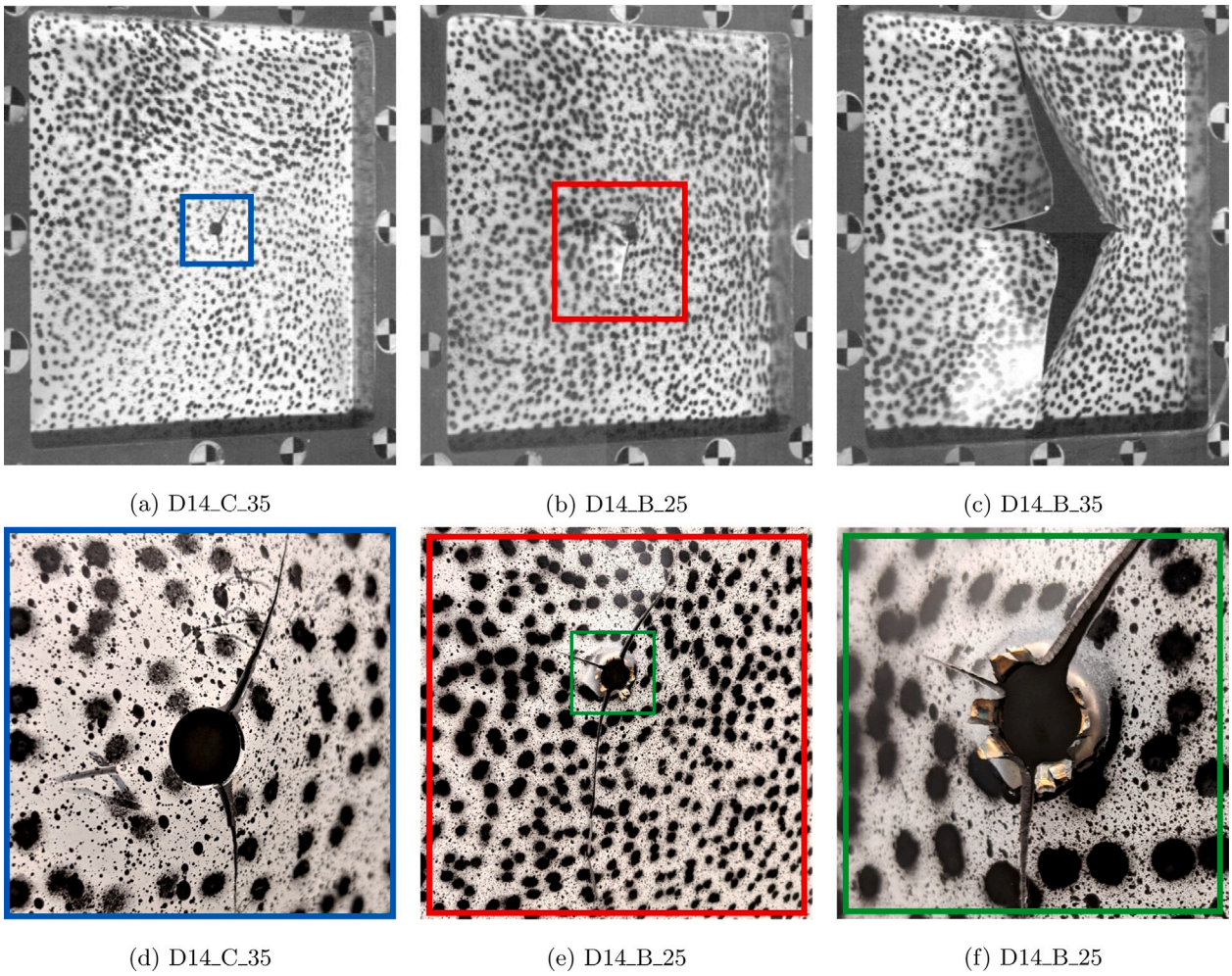

Fig. 8. Pictures of the final state after blast loading for all D14 plates experiencing cracking. The full blast exposed area is given in (a)–(c), and zoomed-in views of the arrested cracks are given in (d)–(f). The test names are given in the subcaptions. Note that (f) gives a zoomed image of the green square in (e). (For interpretation of the references to colour in this figure legend, the reader is referred to the web version of this article.)

where D is the damage indicator defined in the range [0,1], σ_1 is the major principal stress, and dp denotes the equivalent plastic strain increment. As W_c defines the critical damage for a given material, fracture emerges when the damage parameter D reaches unity. However, the major principal stress may be rewritten in terms of the stress triaxiality, σ^*, the Lode parameter, μ_σ, and the flow stress. By substituting the alternative form of σ_1 into Eq. (4) and assuming a yield surface exponent of a = 2, we get

$$D = \frac{1}{W_c}\int_0^p \langle\, \sigma^* + \frac{3-\mu_\sigma}{3\sqrt{3+\mu_\sigma^2}}\rangle \sigma_{\text{eq}} dp \tag{5}$$

where

$$\sigma^* = \frac{\sigma_1+\sigma_2+\sigma_3}{3\sigma_{\text{eq}}}, \qquad \mu_\sigma = \frac{2\sigma_2-\sigma_1-\sigma_3}{\sigma_1-\sigma_3} \tag{6}$$

From Eq. (5) it is observed that the CL damage accumulation represents the plastic work per unit volume, multiplied by a factor depending on the stress triaxiality and the Lode parameter. The damage evolution rate decreases with a decrease in the stress triaxiality, and for sufficiently low values of σ^*, or if $\sigma_1 \leq 0$, no damage is accumulated.

4.2. Identification of material parameters

The constitutive relation described by Eqs. (1)–(4) was implemented as a user-defined subroutine in LS-DYNA. The work hardening parameters Q_i and C_i were obtained through inverse modelling of the uniaxial tension tests, where the measured engineering stress–strain curves were used as target curves in an optimization using LS-OPT. All numerical tension tests applied element type 1, which is the most time efficient and default solid element for explicit simulations in LS-DYNA. This element is formulated as a constant stress hexahedron utilizing a reduced integration [40]. The test specimen was discretized with an element size of 0.2 mm, corresponding to 4 elements over the thickness. An identical element size and element type were used for all simulations throughout this study.

The CL fracture parameter W_c was extracted by following the critical element in the through-thickness centre of the tensile test simulations. This element is exposed to the largest equivalent plastic strain, and at the instant of fracture in the engineering stress–strain curves from the tests for all three materials, W_c was found by integration using Eq. (4). Numerically obtained engineering stress–strain curves are given in Fig. 9(a), with the corresponding CL integrals in Fig. 9(b). The estimated work hardening parameters are summarized in Table 4. Typical elastic and thermal material parameters from the literature were used for all three steels, i.e., E = 210 GPa, ν = 0.33 and ρ = 7850 kg/m^3, while the specific heat capacity was set to C_p = 452 J/kg K, the melting temperature to T_m = 1800 K and the reference temperature to T_r = 293 K.

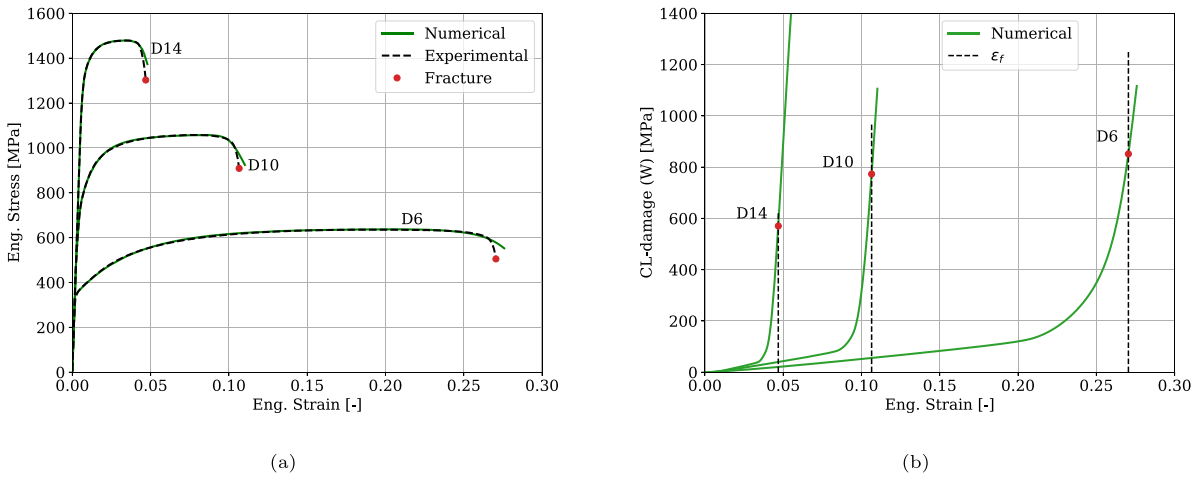

Fig. 9. Comparison of numerically and experimentally obtained engineering stress–strain curves in (a), and the corresponding Cockcroft–Latham (CL) damage evolution in (b).

Table 4
Parameters for the constitutive relation described in Eqs. (1)–(4). All tension tests were performed with a nominal strain rate of $\dot{p}_0 = 5 \times 10^{-4}$ s^{-1}. Both c and m are taken from [29].

Material	A [MPa]	Q_1 [MPa]	C_1 [–]	Q_2 [MPa]	C_2 [–]	Q_3 [MPa]	C_3 [–]	c [–]	m [–]	W_c [MPa]
D6	300.0	43.8	17642.7	275.0	28.5	942.4	0.9	0.01	1.0	851.4
D10	468.8	240.9	1340.5	289.8	118.1	245.0	11.7	0.008	1.0	773.6
D14	1114.8	180.0	1744.7	187.7	185.8	118.1	17.5	0.004	1.0	570.2

4.3. Numerical modelling of fracture

Ballistic impact and blast loading correspond to significantly different stress states during the plastic straining to fracture. By assuming proportional loading conditions, i.e., σ^* and μ_σ remains constant throughout the entire loading history to fracture, the fracture strain p_f may be determined as a function of σ^*, μ_σ, and the obtained material parameters, Q_k, C_k, and W_c by use of the CL failure criterion. The corresponding fracture loci are plotted for all three materials in Fig. 10(a–c). The fracture strain is plotted as a function of σ^* for three given values of the Lode parameter. It is noted that $(\mu_\sigma, \sigma^*) = (-1, 1/3)$ corresponds to generalized tension ($\sigma_1 \geq \sigma_2 = \sigma_3$), $(\mu_\sigma, \sigma^*) = (0,0)$ represents generalized shear ($2\sigma_2 = \sigma_1 + \sigma_3$), $(\mu_\sigma, \sigma^*) = (1, -1/3)$ represents generalized compression ($\sigma_1 = \sigma_2 \geq \sigma_3$), while $(\mu_\sigma, \sigma^*) = (1, 2/3)$ implies biaxial tension ($\sigma_1 = \sigma_2 \geq \sigma_3 = 0$). As the CL failure criterion is driven by positive values of σ_1, the lowest fracture strain is found for generalized tension. Accordingly, the largest fracture strain occurs in generalized compression, and shear ends up in between. Independent of the Lode parameter, the fracture strain increased dramatically with a decrease in stress triaxiality. With sufficiently low stress triaxialities, the fracture strain approaches infinity, and the CL criterion will no longer result in fracture.

Ballistic impacts tend to give compression dominated loading paths for elements in direct contact with the projectile. In such loading cases, the CL failure criterion may result in a highly increased fracture strain for certain elements. To overcome this issue, an additional effective fracture strain ε_{eff} was introduced in the fracture model.

$$\varepsilon_{\text{eff}} = \sqrt{\frac{2}{3}\varepsilon_{ij}^{\text{dev}}\varepsilon_{ij}^{\text{dev}}} \tag{7}$$

where $\varepsilon_{ij}^{\text{dev}}$ represents the deviatoric strain tensor. Hence, the strain-based failure criterion in Eq. (7) will basically erode severely distorted elements. It should be noted that LS-DYNA also allows for eroding elements based on the plastic strain p. Preliminary simulations showed more or less the same predictions of element erosion when using thresholds of p that were slightly smaller than ε_{eff}.

It was therefore decided to use the same strain-based criterion as in Refs. [41,42], where elements were eroded if the effective von Mises strain ε_{eff} from Eq. (7) reached a given threshold. However, for the particular case of the ballistic impact simulations under consideration in this study, it is reasonable to assume that $\varepsilon_{\text{eff}} \approx p$ because the loading monotonically increases during the perforation process. Moreover, the assumption of a Hershey yield surface in Eq. (2) and that the plastic flow is given by the associated flow rule imply a plastically incompressible behaviour of the material. Hence, only deviatoric strains ($\varepsilon_{ij}^{\text{dev}}$) will contribute to the accumulated plastic strain. Volumetric strains are therefore limited to the elastic part of the material model. Thin plates experiencing large deformations have negligible elastic volumetric strains and the material behaviour is therefore assumed to be governed by deviatoric strains.

The additional fracture strain can therefore be interpreted as a "capping" of the CL fracture loci at low triaxialities. The "capping" is visualized as the green dotted lines in Fig. 10.

In Fig. 10(d), the loading paths for the most damaged element in the numerical tension tests are plotted for all three materials. During the numerical tension tests, both the stress triaxiality and the Lode parameter are changing, and these curves are hence not directly comparable to the fracture loci in Fig. 10(a–c). For all three materials, the stress triaxiality lies between 0.32 and 0.62, and the corresponding Lode parameter is between −1 and −0.4, which places the fracture strain around the lower right portion of the loci.

Fig. 11 presents results from numerical simulations using the specimen geometry in Fig. 1(b) and the material parameters in Table 4. The results are presented as the damage field in Fig. 11(a) at the instant of fracture initiation for the three materials under consideration, while the analytical expression of the work hardening $R(p)$ is plotted against the plastic strain p in Fig. 11(b). It is evident that the three materials are experiencing distinct differences in the ability to distribute the damage over the gauge area of the specimen geometry. While D14 experiences a strong localization of plastic deformation and damage, D6 and D10 are gradually distributing the damage across a larger area. It is interesting to note the correlation between localization of damage in Fig. 11(a) and work hardening characteristics in Fig. 11(b). That is, increased work hardening distributes the plastic deformations and the corresponding damage over a much larger area. In turn, this leads

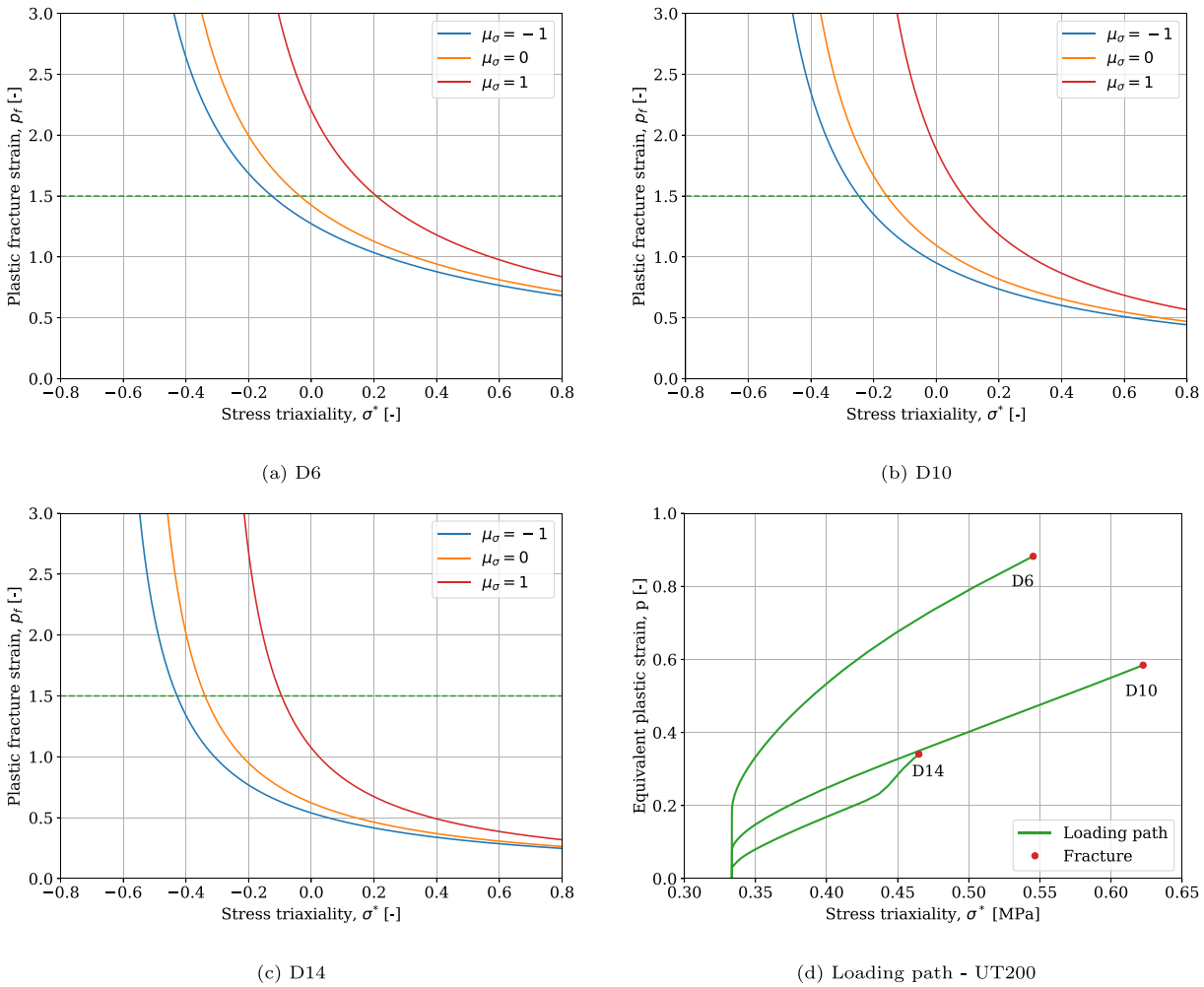

Fig. 10. (a–c) Fracture loci based on the CL failure criterion for all materials at selected values of the Lode parameter, (d) the loading path to fracture for the most damaged element in the simulations of the tension tests are plotted for all materials. (For interpretation of the references to colour in this figure legend, the reader is referred to the web version of this article.)

to a larger dissipation of plastic work and an increased resistance to fracture and crack propagation. The main trend is that the increased material strength leads to a reduction in work hardening, confirming the observations on the strength-ductility trade-off in Ref. [27].

5. Numerical simulations of combined ballistic impact and blast loading

Numerical simulations were used to gain more insight into the fracture characteristics of pre-damaged plates exposed to blast loading. However, before moving into the detailed simulations of the blast loaded plates, it is necessary to address some challenges in the numerical modelling and simulation of scenarios involving combined ballistic impact and blast loading.

5.1. Numerical model

To replicate the experimental tests, the ballistic impact and blast simulation were run in two separate analyses. This was formulated as a full deck restart analysis in LS-DYNA, using a **DAMPING_PART_MASS* numerical damping in between the two load cases to minimize elastic oscillations prior to the blast load.

The numerical model is shown in Fig. 12. The experimental setup allowed for the use of two symmetry planes. The clamping assembly consists of two steel plates which are coloured with green and brown in the figure, and 3 bolts (2 full and 2 half). Both the bolts and the green clamping frame are fixed for translation in all directions along the surface facing outwards in Fig. 12(c). The target plate and the brown clamping frame are constrained by contact with the surrounding parts. As shown in Fig. 12(c), the blast-exposed surface of the target plate is bounded by the inner square of the green clamping frame. The clamping frame and bolts were modelled as elastic (*MAT_001), using standard material parameters for steel. The constitutive relation and material parameters applied for the target plates are described in Section 4.1.

The overall aim of the ballistic simulations was to predict a realistic fracture mode in the target plates. That is, to obtain a realistic starting point for the blast simulations in terms of the number of petals and initial cracks from the ballistic impact. Hence, the ballistic resistance of the target plates was not considered in detail. As no visual deformation or damage was observed for the projectiles in the experiments, rigid projectiles were applied in the numerical models. The projectiles were given an initial velocity of 900 m/s. The quarter symmetry of the target plate assembly was also adopted for the projectile.

During a ballistic impact, the localized area in which the material fails experiences high pressures, leading to low stress triaxialities. As a consequence, the CL failure criterion (Eq. (5)) accumulates no damage in these elements under compressive stress states although there are significant plastic deformations. Numerically, this allows for elements to

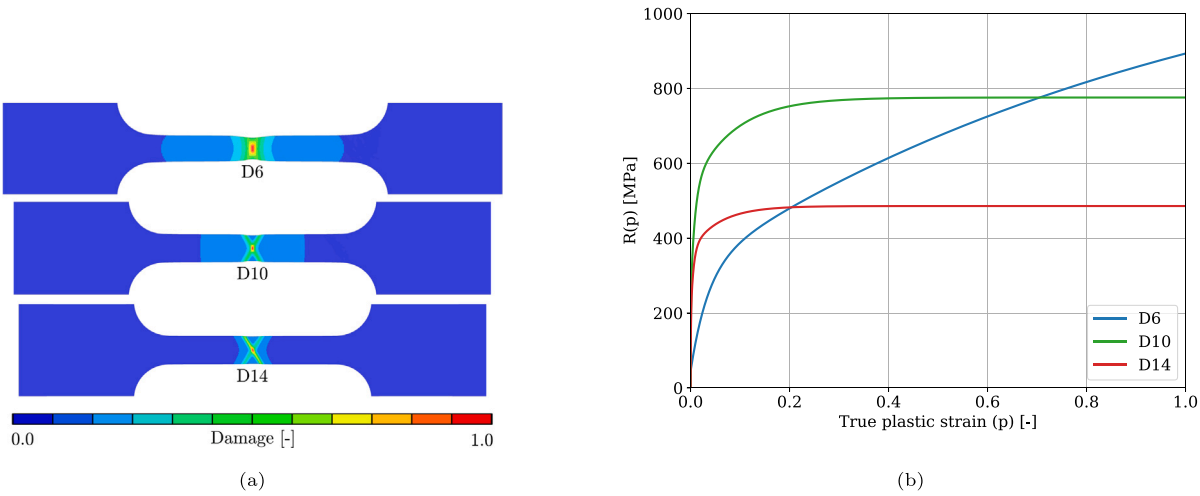

Fig. 11. Numerical modelling of the three materials under consideration: (a) Damage fields extracted at the instant of fracture, and (b) the analytical expressions for the work hardening $R(p)$ when using the Voce parameters in Table 4. The damage fields is based on the CL criterion in Eq. (4).

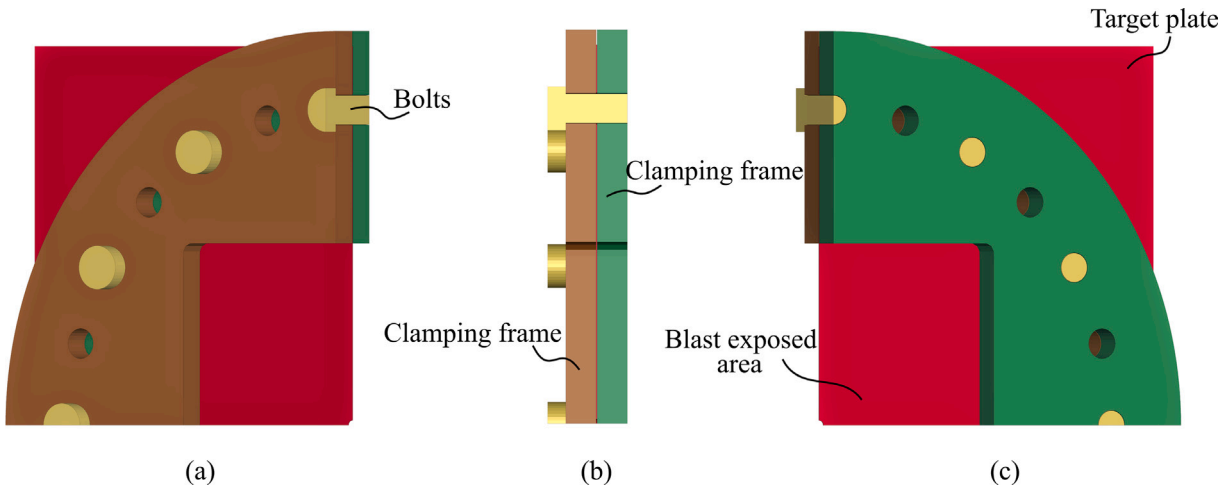

Fig. 12. The numerical model of the clamping assembly and the target plate: (a) a view of the unloaded surface, (b) seen from the side, and (c) a view of the blast-exposed surface. It is noted that quarter symmetry has been utilized. (For interpretation of the references to colour in this figure legend, the reader is referred to the web version of this article.)

exhibit excessive plastic deformation without failing [38]. If adiabatic heating is included, the localized areas of large plastic deformations and high plastic strain rates will experience significant heating and the element could therefore be eroded due to a temperature-based failure criterion. However, the local plastic deformation and corresponding adiabatic heating of each element within the impact zone is very mesh sensitive [23]. Simulations with a sufficiently fine mesh using 3D brick elements is considered as unrealistic in the context of combined ballistic impact and blast loading. This presents a challenge on how to model such a loading event, because refining the mesh is not feasible within the scope of this work.

Alternative modelling approaches to handle excessively distorted elements with low CL damage accumulation in ballistic impact simulations are typically to either erode elements if the critical time step drops below a given threshold or at a given strain limit. In this study it was decided to adopt an additional strain-based erosion criterion from Refs. [41,42], where elements are eroded if the effective von Mises strain ε_{eff} from Eq. (7) reaches a given threshold. This is governed by the *EFFEPS* keyword in the **MAT_ADD_EROSION* module in LS-DYNA. To introduce an additional strain-based failure criterion is somewhat similar to capping the fracture locus, as illustrated in Fig. 10. It is important to note that this was only applied during the ballistic impact simulations, and not in the subsequent blast simulations. Fracture in the blast simulation was governed solely by the CL failure criterion and the critical temperature.

Aune et al. [16] studied blast-loaded steel plates of similar dimensions as those used in this study. It was shown that a discretization consisting of 0.8 mm shell elements for the target plates gave an accurate description of both plastic deformations and fracture during blast loading. However, shell elements cannot be used in the ballistic impact simulations. As a compromise between numerical accuracy during ballistic impact and computational efficiency during blast loading, it was decided to apply a uniform mesh of 0.2 mm solid elements. This corresponds to 4 elements across the plate thickness. All blast simulations in this study used the idealized pressure histories from Aune et al. [32] shown in Fig. 13. It is noted that the applied pressure histories are obtained in separate experiments obtaining pressure measurements on the blast-exposed surface of a massive, non-deformable steel plate. This gives a conservative estimate of the loading history, as FSI effects are expected to somewhat lower the blast pressure for thin steel plates [34].

The two loading cases are evaluated separately with the ballistic impact simulations in Section 5.2, and the blast simulations in Section 5.3. More specific information regarding the modelling of the two loading cases are given within the respective sections.

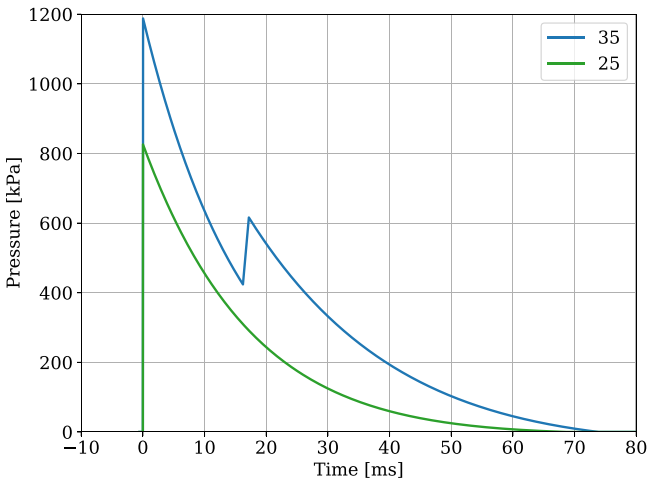

Fig. 13. The pressure histories used in the blast simulations.

5.2. Numerical results for ballistic impact

The goal of this study is to investigate the influence of ballistic impact on the blast resistance of thin steel plates. Thus, the simulations of the ballistic impacts are conducted to generate similar petalling cracks as those seen in the physical tests as a starting point for the subsequent blast simulations. It was therefore considered necessary to carry out a parametric study on the influence of the threshold value of the effective fracture strain, ε_{eff} in Eq. (7), on the simulated petalling mode. This was done using three different thresholds of ε_{eff} for each material. It was decided to apply the same three thresholds for all three materials under consideration, i.e., 1.0, 1.5, and 2.0. As a reference, one simulation of each material excluding the strain-based failure criterion was also performed (i.e., $\varepsilon_{\text{eff}} = 0.0$). The corresponding numerical results are given for plates of D6, D10 and D14 in Fig. 14. It is noted that the quarter model was mirrored across the two symmetry planes in the ballistic holes for a better visualization. The applied level of ε_{eff} is given above each subfigure. The total number of eroded elements for each simulation is given at the bottom of each figure.

For all three materials, simulations where element erosion is based solely on the CL failure criterion and the critical temperature do not resemble the fracture mode observed in the physical tests, as seen in Fig. 4. No distinct petals or cracks are formed around the bullet hole, and highly distorted elements with a low damage accumulation occur in the periphery of the holes. As ε_{eff} approaches a threshold of 1.0, the obtained fracture mode is more similar to the experimental observations, and the number of eroded elements are increasing for all three plate materials. The improved results and increased number of eroded elements with the additional strain-based failure criterion indicate that the CL failure criterion and critical temperature alone are not able to describe the physical mechanisms leading to fracture for the applied mesh.

Fig. 14 shows that the D14 plate gave the largest number of eroded elements. This is reasonable as D14 is the material with the smallest amount of both ductility and hardening (see Figs. 9 and 11). It is also seen that the strain-based erosion criterion affects the interaction between the projectile and the target plate. As the elements in contact with the projectile are eroded early in the perforation process, the threshold for ε_{eff} will determine the ballistic hole geometry. Even though the D14 plates were the least sensitive to variations in the effective failure strain, the number of petals increased with almost a factor of 2 from $\varepsilon_{\text{eff}} = 1.0$ to $\varepsilon_{\text{eff}} = 1.5$. This effect was not found for the D6 and D10 simulations, where distinct petals mainly occurred for $\varepsilon_{\text{eff}} = 1.0$.

To better understand the need to include an additional strain-based failure criterion for the ballistic impact simulations, it was decided to study the stress state in selected elements in the simulations without the strain-based erosion criterion. The elements were selected based on their position across the plate thickness and with respect to the distance from the projectile nose. Fig. 15 shows the selection of elements. Hence, the elements across the thickness were evaluated at two separate distances from the plate centre along one of the symmetry lines in the quarter model. The corresponding plots of the stress triaxiality and the damage (see Eq. (4)) shown in Fig. 16 follow the same colour convention for each elements as indicated in Fig. 15. As all three materials showed similar trends, it was decided to only present the stress triaxiality and damage for the D14 material.

From the plots of the stress triaxiality in Fig. 16(a) and (b), it is observed that the stress state for the impacted elements is compression dominated. This is particularly the case for the elements in the upper half of the plate thickness (Elements 1 and 2). As Element 1 is in direct contact with the projectile and Element 4 lies on the opposite side of the plate thickness, it is reasonable that the stress triaxiality is increasing from Element 1 to Element 4. By considering the corresponding plots of the damage in Fig. 16, the negative triaxialities translate to large plastic straining without any accumulation of damage. From Fig. 16(a) and (b) it is also seen that the stress triaxiality is decreasing, while Fig. 16(c) and (d) indicates that the fracture strain is increasing as the distance to the plate centre is decreased. Some elements closer to the centre than the evaluated elements experienced plastic strains above 3 without exceeding the CL criterion in Eq. (4).

It should also be noted that a mesh refinement corresponding to 8 elements across the thickness (element size of 0.1 mm) was also used in an attempt to improve the simulations of the fracture mode. However, even at this element size the fracture modes were poorly represented when using only the CL failure criterion and the critical temperature. Fig. 16(a) and (b) show that the simulations of the ballistic impact resulted in stress triaxialities as low as −1.5 for a large portion of the critical elements. Even the major principal stress turned negative and no accumulation of damage occurred. Hence, it is found necessary to use an additional failure criterion to predict realistic fracture modes during ballistic impact on a course mesh, motivating the use of the strain-based criterion in Eq. (7). Another alternative would be to use a more advanced fracture criterion that better accounts for damage at lower stress triaxialities. However, this is beyond the scope of this study.

5.3. Numerical results for blast loading simulations

The numerical results of the blast simulations are divided into two main parts. First, the global response is evaluated for simulations that do not show any sign of fracture. Secondly, the fracture resistance in the different materials and plate geometries are considered.

5.3.1. Global response

The permanent out-of-plane displacement fields of plates with a pre-cut circular hole (C) are presented in Fig. 17. It is noted that only results from the lowest blast intensity and the C geometry are presented in this section, as this is the only configuration where none of the materials experienced any fracture. As in the physical tests (see Fig. 6(a–c)), the permanent deformations are decreasing with increasing material strength and the distribution of deformations gets more localized around the centre for the D10 and D14 plates. However, increased magnitudes of permanent deformations are seen in the numerical simulations compared to the experimental observations. This was expected because the simulations are neglecting FSI effects, and the applied pressure histories are obtained in separate tests on rigid target plates. This will overestimate the deformations [16,34].

Fig. 18 provides the equivalent plastic strain p when the plates have reached the permanent deformed configuration. It is evident

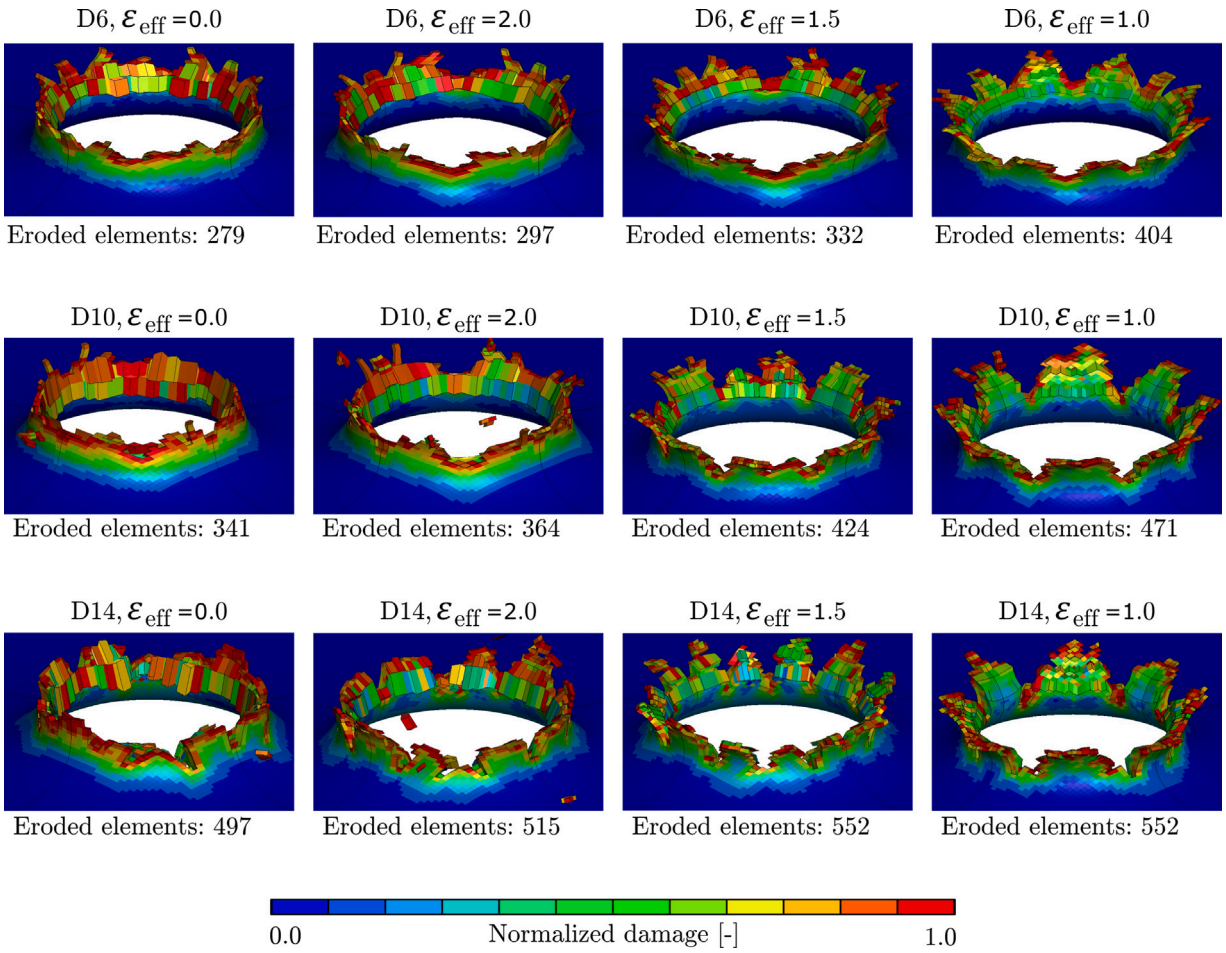

Fig. 14. Numerical results for all ballistic impact simulations. The three different thresholds of the effective strain erosion criterion (ε_{eff} in Eq. (7)) are given at the top of each figure for each material. ε_{eff} = 0.0 denotes the simulation where only the CL failure criterion and critical temperature were applied. Note that the quarter model was mirrored across the two symmetry planes for a better visualization. The total number of eroded elements for each simulation is given at the bottom of each figure.

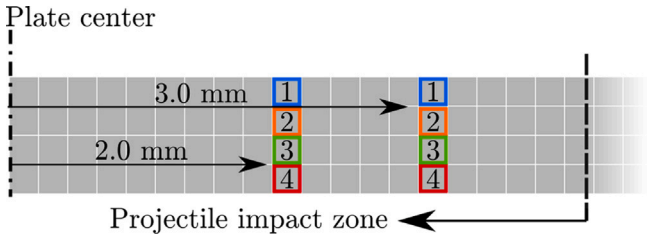

Fig. 15. The selection of elements used for the evaluation of the stress state during ballistic impact. The cross section represents the plate thickness along one of the symmetry planes, where the left end represents the plate centre. The projectile impacts the entire region called the "Projectile impact zone". The element IDs used in Fig. 16 are indicated inside each element. (For interpretation of the references to colour in this figure legend, the reader is referred to the web version of this article.)

that the magnitude of the plastic strains are significantly larger for the D6 plate, compared to the D10 and D14 plates. The maximum plastic strain occurred at the periphery of the pre-cut hole for all tests, with a magnitude of 0.23 for D6_C_25 (Fig. 18(a)), 0.13 for D10_C_25 (Fig. 18(b)), and 0.12 for D14_C_25 (Fig. 18(c)). However, the most dominant difference in the equivalent plastic strain fields is the difference in distribution. For the most ductile plate (i.e., D6_C_25), the plastic strains are distributed across a large area around the centre of the target plate. As the ductility is reduced and the strength increased, D10_C_25 experiences a more localized distribution around the plate centre. This effect is even more evident for test D14_C_25. Within the areas of localized plastic strain, some clear differences are seen between the three materials when considering the zoomed images of the pre-cut holes in Fig. 18. For D6_C_25, the strongest localization occurred as a circular area along the periphery of the pre-cut hole. A similar distribution is seen for D10_C_25. For D14_C_25, distinct localizations have formed along the diagonals. The comparison of the plastic strain distributions in Fig. 18 resembles the same trends that were observed in the simulations of the uniaxial tension tests in Fig. 11(a), where localization occurred at smaller strains for the D14 material compared to the D6 and D10 materials.

When the blast intensity was increased in the simulations, both D6_C_35 and D10_C_35 resulted in increased deformations, but no signs of fracture were found. As in the experiments, D14_C_35 experienced fracture in the numerical model. In the experiments, two large arrested cracks were observed, while the numerical model ended with complete tearing where the cracks initiated and propagated along the diagonals and all the way to the clamping frame.

5.3.2. Fracture resistance

As in the physical tests in Section 3.4, the numerical simulations showed that the blast resistance was strongly dependent on the fracture mode from the ballistic impact. The final state of crack propagation is given for tests D6_B_35 and D10_B_35 in Fig. 19. Quarter symmetry was applied in all blast simulations, and all images have been mirrored across the two symmetry planes for a better visualization. It is emphasized that the strain-based failure criterion (ε_{eff}) in Eq. (7) was only applied during the ballistic impact simulations and was not used

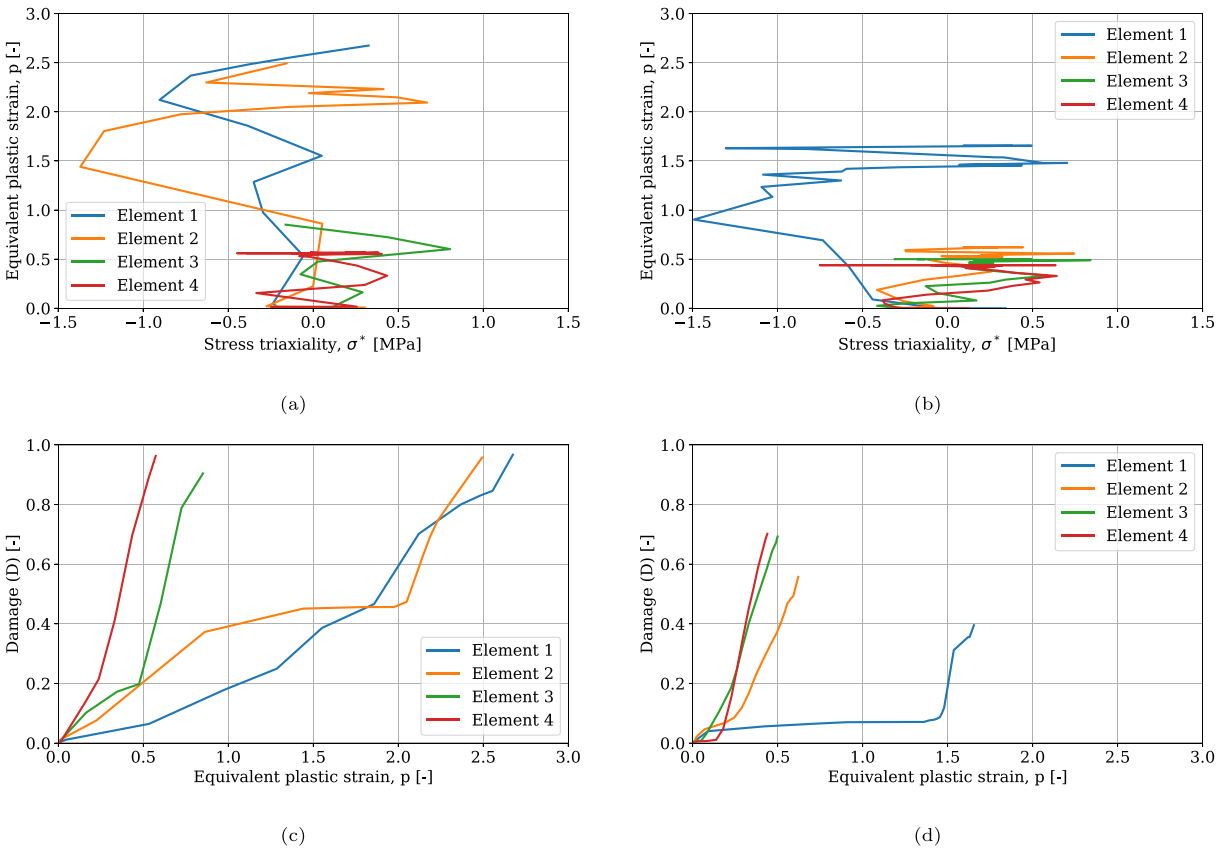

Fig. 16. The stress triaxiality versus the equivalent plastic strain in the elements indicated in Fig. 15: (a) the elements at a distance of 2.0 mm from the plate centre, and (b) the elements at a distance of 3.0 mm from the plate centre. The equivalent plastic strain versus the accumulated damage in the elements indicated in Fig. 15: (c) the elements at a distance of 2.0 mm from the plate centre, and (d) the elements at a distance of 3.0 mm from the plate centre. As all three materials resulted in similar trends, only the results for the D14 material are presented. (For interpretation of the references to colour in this figure legend, the reader is referred to the web version of this article.)

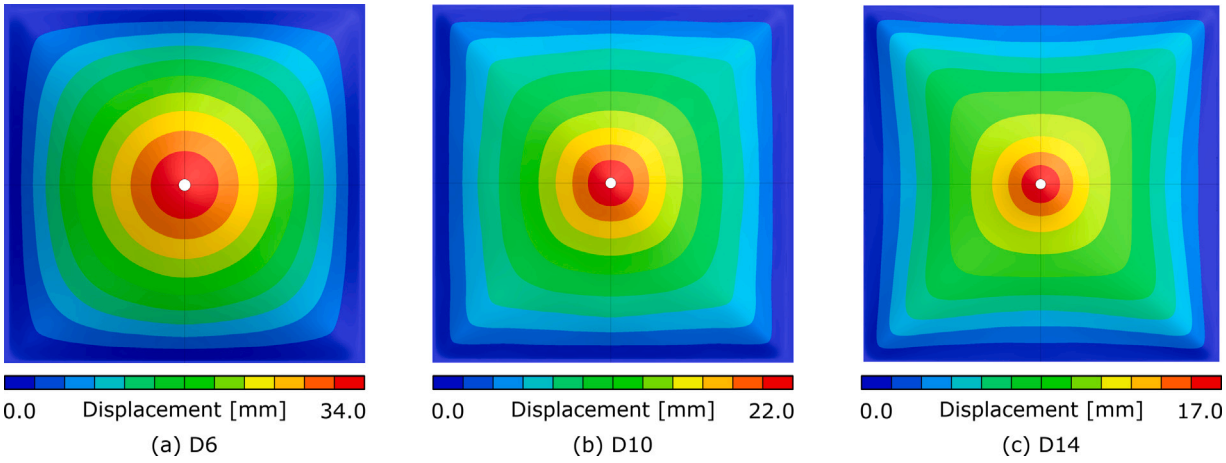

Fig. 17. The permanent out-of-plane displacement fields from numerical simulations of plates with a pre-cut circular hole (C), exposed to the lowest blast intensity. The plate materials are indicated in the sub-caption of each image. Note that the quarter model was mirrored across the two symmetry planes for a better visualization.

in the blast load simulations. Hence, the fracture during blast loading was only governed by the CL failure criterion in Eq. (4) and possible thermal effects.

As shown in Section 5.2, the fracture mode during the ballistic impact was sensitive to variations in the fracture strain. A successful result in predicting the petalling cracks for the D6 and D10 plates where obtained using $\epsilon_{\text{eff}} = 1.0$. The absence of fully formed petals will influence the blast simulations such that the response is more similar to the target plates with pre-cut circular holes. The CL damage fields given for tests D6_B_35 and D10_B_35 in Fig. 19 are therefore restarted from the ballistic simulations using $\epsilon_{\text{eff}} = 1.0$. The lengths of the arrested cracks in the D6_B_35 and D10_B_35 simulations were measured to be of similar magnitude as what was found for the corresponding blast tests. However, the D6_B_35 and D10_B_35 tests resulted in only 2 and 3 arrested cracks, respectively. As the numerical models applied quarter symmetry, one crack in the quarter model corresponds to 4 cracks for the full geometry. This means that the numerical simulations predict a larger crack length than that observed in the physical tests.

Fig. 20 shows the final states of crack propagation for test D14_B_25. Two alternative results are given, due to the findings in Section 5.2

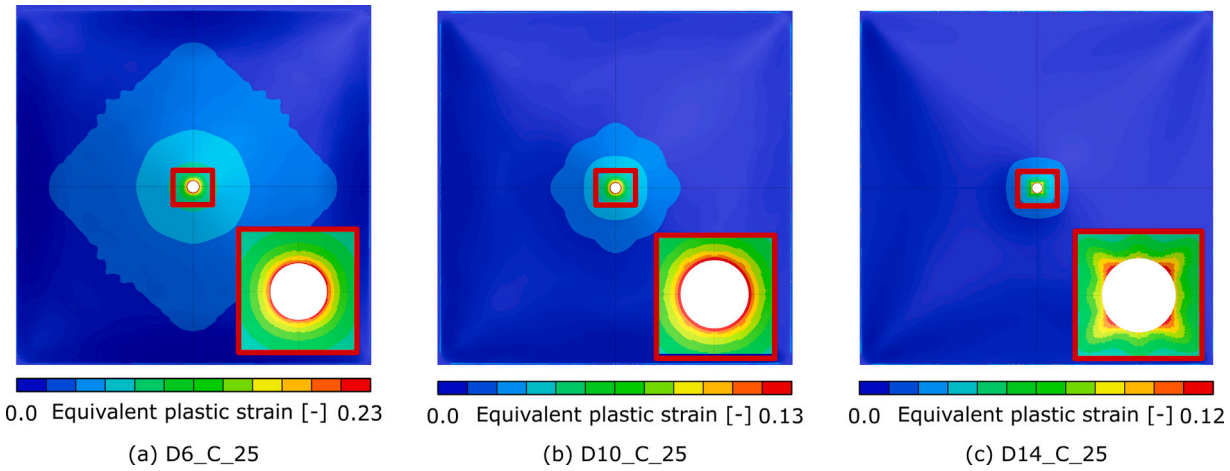

Fig. 18. The equivalent plastic strain fields corresponding to the state of permanent deformation. Zoomed images of the plastic strain distribution around the pre-cut holes are given in the lower right corner of each figure, indicated with a red square. The test names are given in the sub-captions. Note that the quarter model was mirrored across the two symmetry planes for a better visualization. (For interpretation of the references to colour in this figure legend, the reader is referred to the web version of this article.)

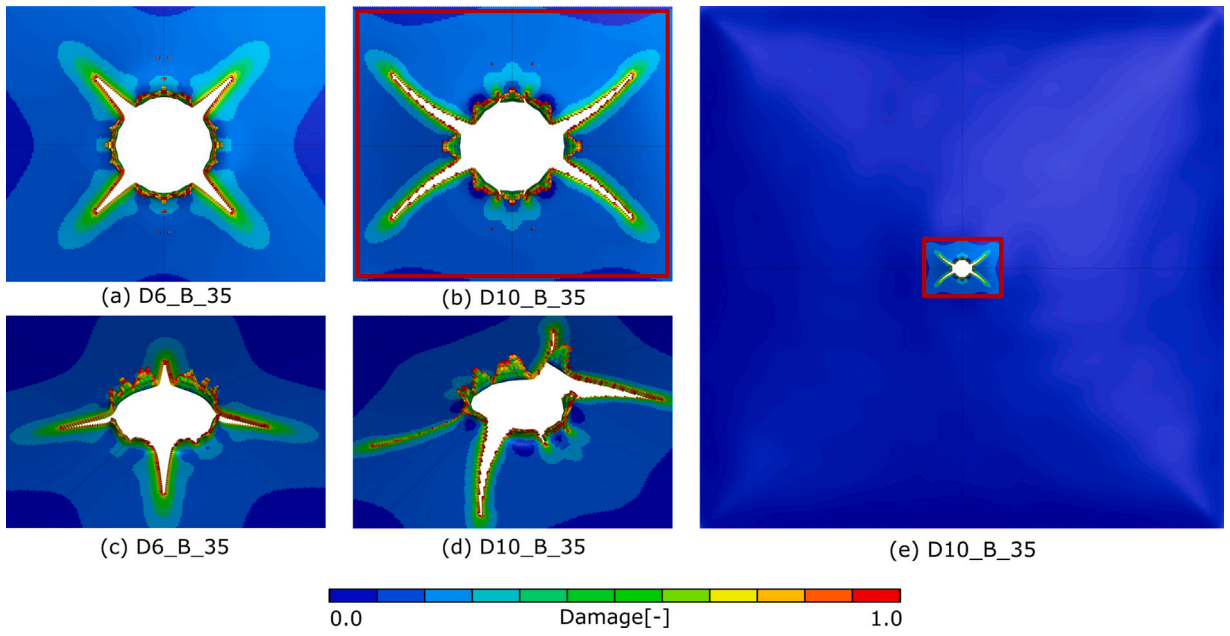

Fig. 19. Final state of arrested cracks for D6_B_35 in (a) and (c). D10_B_35 is shown in (b), (d), and (e). The full geometry of the blast exposed area is indicated in (e) to visualize the correct scale and proportion of the arrested cracks. Simulation identities are indicated in the subcaptions.

where both threshold values of $\varepsilon_{\text{eff}} = 1.0$ and $\varepsilon_{\text{eff}} = 1.5$ predicted reasonable petalling cracks during the ballistic impact of the D14 plates. This allowed for a numerical study on the influence of the number of petalling cracks on the blast resistance of the D14 plates. The blast simulations starting from the ballistic simulations with $\varepsilon_{\text{eff}} = 1.0$ contained approximately half the number of petals compared to those starting from ballistic simulations using $\varepsilon_{\text{eff}} = 1.5$. It should also be noted that $\varepsilon_{\text{eff}} = 1.5$ have petalling cracks aligned with the plate diagonals, while $\varepsilon_{\text{eff}} = 1.0$ only have vertical and horizontal petalling cracks.

From Fig. 20 it is clear that the two different petalling distributions ($\varepsilon_{\text{eff}} = 1.0$ and $\varepsilon_{\text{eff}} = 1.5$) for test D14_B_25 resulted in two different fracture patterns during blast loading. The blast simulation starting from the ballistic impact using $\varepsilon_{\text{eff}} = 1.0$ resulted in short arrested vertical cracks (Fig. 20(a),(c)), while blast simulations starting from the ballistic results using $\varepsilon_{\text{eff}} = 1.5$ gave significantly longer cracks along the plate diagonal (Fig. 20(b),(d)). All cracks are initiated at the petals resulting from the ballistic impact event. It is noted that both simulations resulted in smaller arrested cracks than in the physical tests. Both blast simulations of test D14_B_25 applied identical blast intensity and material parameters. The only difference between the two models in Fig. 20 is the fracture mode from the ballistic impact. Hence, it is evident that the crack initiation and crack propagation during blast loading are sensitive to the petalling distribution and orientation from the ballistic impact.

Fig. 21 provides representative crack propagation paths for simulations of the D14 plate exposed to the highest blast intensity. The results for test D14_C_35 are given in Fig. 21(a), while the results for the two petalling modes for test D14_B_35 are given in Fig. 21(b) and (c). As the pre-cut circular hole (C) geometry in test D14_C_35 represents an ideal geometry, this simulation will also serve as a basis of comparison to evaluate the effect of the petalling mode in the crack initiation and propagation during the blast loading phase. Thin, square plates subjected to blast loading are expected to experience cracks propagating along the plate diagonals (see e.g., Refs. [16,20,27,36]). Both D14_C_35 and D14_B_35 - $\varepsilon_{\text{eff}} = 1.5$ ended in total fracture, with

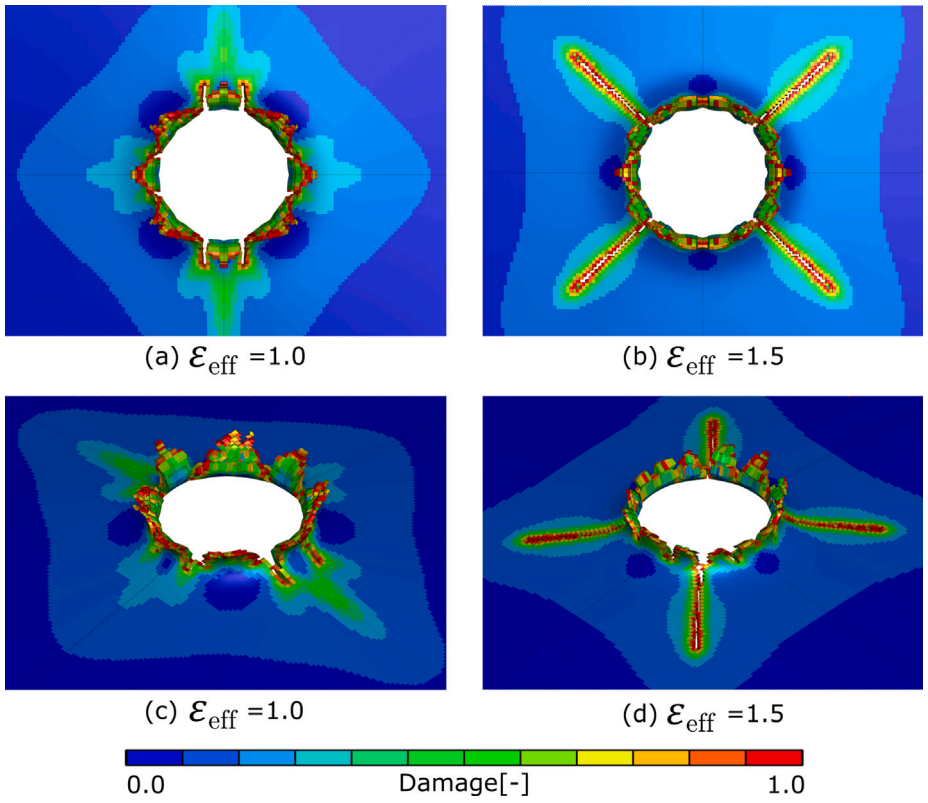

Fig. 20. Final state of arrested cracks for D14_B_25 based on two different fracture strain thresholds from the ballistic impact. The blast simulation restarted from $\varepsilon_{\text{eff}} = 1.0$ is given in (a) and (c), while the simulation restarting from $\varepsilon_{\text{eff}} = 1.5$ is given in (b) and (d). It is noted that the values of ε_{eff} are referring to the additional strain-based failure criterion during ballistic impact, as this strain criterion was not included in the blast simulations.

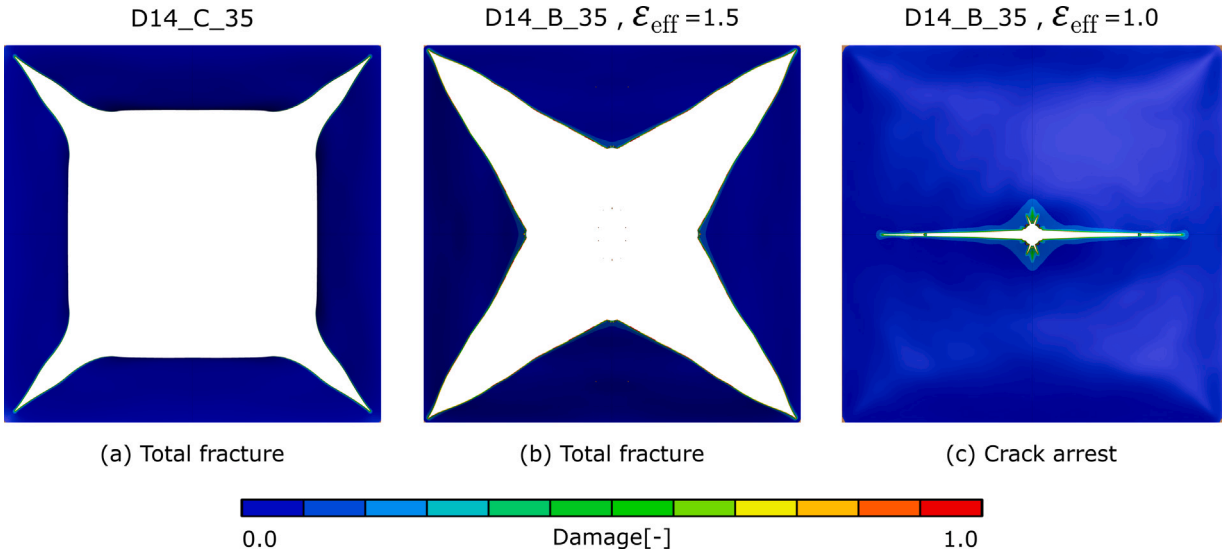

Fig. 21. The final state of crack propagation from blast simulations for test D14_C_35 is shown in (a), while similar results from blast simulations with two different petalling modes from the ballistic simulations for test D14_B_35 are shown in (b) and (c). Note that ε_{eff} refers to the two different thresholds used for the strain-based failure criterion in the ballistic impact simulations. The strain-based failure criterion was not included in the blast simulations. It is stated in the subcaptions weather the simulation ended in crack arrest or total fracture.

cracks propagating along the diagonals. However, D14_B_35 - $\varepsilon_{\text{eff}} = 1.0$ corresponds to another petalling mode than $\varepsilon_{\text{eff}} = 1.5$, and resulted in significant arrested cracks along the horizontal direction. This means that the change in petalling mode from $\varepsilon_{\text{eff}} = 1.5$ to $\varepsilon_{\text{eff}} = 1.0$ changed the direction of crack propagation during blast loading, and hence increased the resistance to fracture of the target plate.

Another interesting observation is the discrepancy in numerically predicted crack resistance between the different models. All blast simulations resulted in larger cracks than that in the physical tests, except for the blast simulations of the D14 plates with ballistic perforations (i.e., tests D14_B_25 and D14_B_35). Since FSI effects were neglected in this study, the applied loading curves could represent a slightly higher

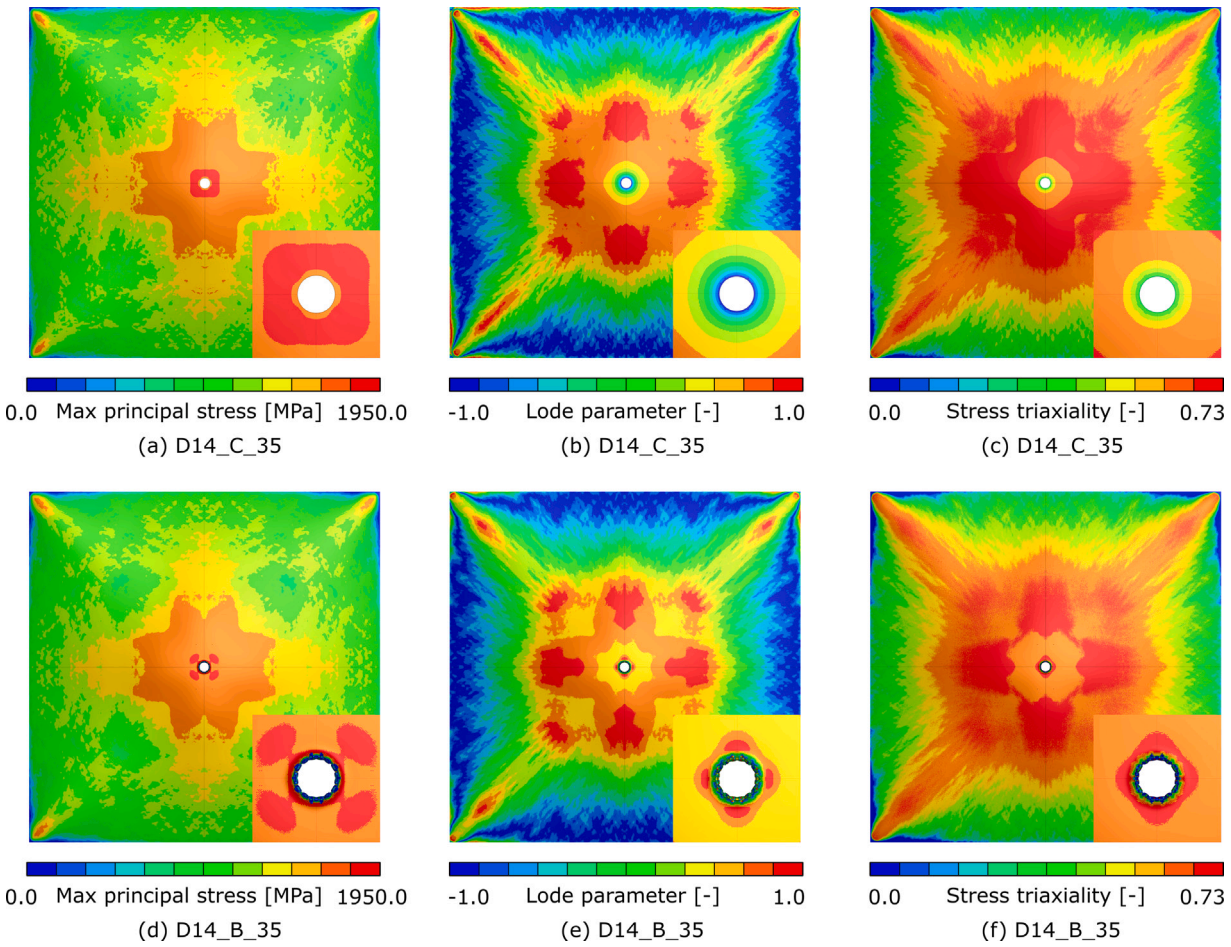

Fig. 22. Field plots of the major principal stress σ_1, the Lode parameter μ_σ, and the stress triaxiality σ^* right before the crack initiation occurred. The D14_C_35 simulation is presented in (a)–(c) and the D14_B_35 simulation in (d)–(f). All field plots are taken from the unloaded surface of the target plates.

blast intensity than that in the actual tests (see Ref. [34]). However, this only explains the simulations giving conservative estimates of the fracture resistance. A plausible explanation for the non-conservative predictions of the fracture resistance in some of the blast simulations with ballistic perforations is the change in crack propagation path. All simulations leading to conservative estimates of the resistance to fracture experienced crack propagations along the plate diagonals. Simulations that overestimated the fracture resistance experienced crack propagation along the vertical and horizontal directions. Thus, the numerical predictions are very sensitive to changes in the petalling modes resulting from the ballistic impact.

5.4. Stress states during blast loading

As the stress states and validity of the CL failure criterion were investigated for the ballistic impact simulations in Section 5.2, this section aims to perform a similar evaluation for the blast simulations. In Fig. 22, the major principal stress σ_1, the Lode parameter μ_σ, and the stress triaxiality σ^*, are presented for two representative blast simulations. The field plots show the unloaded surface of the target plates, and were captured right before crack initiation occurred. A zoomed image around the ballistic impact holes of the target plates is given at the lower right corner of each subfigure.

Overall, it is seen that both σ_1, μ_σ, and σ^* gives similar distributions for the two simulations in Fig. 22. However, some differences are observed around the bullet hole in D14_B_35 compared to the pre-cut circular hole in D14_C_35. For σ_1, which is the driving force in the CL-fracture criterion, a stronger localization along the diagonals is observed for D14_B_35 than for D14_C_35. This is reasonable, as the bullet hole contains small petalling cracks, which generally leads to increased stress concentrations. From the definitions of μ_σ and σ^* in Section 4.3, it is seen in Fig. 22(b) and (c) that the D14_C_35 simulation is experiencing a stress state close to uniaxial tension at the periphery of the pre-cut hole right before crack initiation. The D14_B_35 simulation on the other hand undergoes larger values for both μ_σ and σ^*, yielding a stress state closer to biaxial tension. However, both target plate geometries correspond to stress states within the same range as the uniaxial tension tests applied to determine the CL failure parameter W_c, shown in Fig. 10.

6. Concluding remarks

Experimental and numerical studies were conducted to investigate the effect of ballistic impact prior to blast loading of thin steel plates. This was done by comparing the response of plates with pre-cut circular holes to that of plates with ballistic perforations when exposed to the same blast intensity. Three steel qualities with distinct differences in strength, ductility and work hardening characteristics were tested to get a better understanding of the strength-ductility trade-off. Numerical models were evaluated based on the experimental observations, where special focus was placed on the compromise between computational accuracy during ballistic impact and computational efficiency during blast loading. The numerical simulations were also used to address challenges related to the distinct differences in the loading paths to fracture for both the ballistic impact and the blast loading. The main conclusions from the study are as follows.

- As expected, the ballistic impact resulted in reduced blast resistance compared to the target plates with pre-cut holes. This trend was found for all plate materials, both in the physical tests and in the numerical simulations. Even though the pre-cut circular holes (C) and ballistic holes (B) both were circular with a diameter of about 8 mm, the ballistic impact introduced small petalling cracks and additional damage to the material around the perforation. It was evident that the crack propagation during blast loading was initiated at these petalling cracks. Hence, pre-cut holes containing initial material damage gives a lower fracture resistance than pre-cut circular holes in thin blast-loaded steel plates.
- The three materials evaluated in this study showed a step-wise increase in material strength and a corresponding decrease in ductility. The fracture resistance during blast loading decreased with an increase in material strength. Furthermore, the reduced fracture resistance as a result of the ballistic impact increased with increased material strength. This confirms previous findings on the influence of the strength-ductility trade-off on the fracture resistance of perforated plates, where plates with higher strength are more prone to cracking and fracture than plates with lower strength. Higher material strength typically comes with lower ductility. Thus, this study shows that work hardening and ductility may be more important than the strength for the fracture resistance of pre-damaged and blast-loaded thin steel plates.
- The numerical models were able to capture the main trends observed in the physical tests, i.e., a decrease in blast resistance after ballistic impact and reduced fracture resistance with increased material strength. The most challenging aspect of a successful result in the numerical simulations of combined ballistic impact and blast loading was the representation of the fracture mode during the ballistic impact using a rather course finite element model. Provided a good description of the petalling cracks from the ballistic impact, the numerical simulations of the blast loaded plates predicted the same trends as those observed in the physical tests. The numerical simulations did not succeed in obtaining a good description of the fracture mode in the ballistic impact using the CL failure criterion in combination with a temperature criterion using a course mesh. To capture the experimentally observed petalling cracks during ballistic impact in this study, a strain-based failure criterion was included in addition to the CL failure criterion to erode elements at low triaxialities. The blast simulations only used the CL failure criterion and critical temperature.
- The numerical models of the target plates can be used to gain more insight into the combined effect of ballistic impact and blast loading. It is emphasized that this study is limited to load intensities generated within the capability of a shock tube facility. This motivates further studies on the influence of other load intensities, e.g., those generated by close-in detonations.

CRediT authorship contribution statement

Benjamin Stavnar Elveli: Conceptualization, Methodology, Software, Formal analysis, Investigation, Writing – original draft, Visualization. **Torodd Berstad:** Methodology, Software. **Tore Børvik:** Conceptualization, Methodology, Writing – review & editing, Supervision. **Vegard Aune:** Conceptualization, Methodology, Writing – review & editing, Supervision.

Declaration of competing interest

The authors declare that they have no known competing financial interests or personal relationships that could have appeared to influence the work reported in this paper.

Data availability

Data will be made available on request.

Acknowledgements

This work has been carried out with financial support from NTNU and the Research Council of Norway through the Centre for Advanced Structural Analysis (CASA), Centre for Research-based Innovation (Project No. 237885). The financial support by the Norwegian Ministry of Justice and Public Security is also greatly appreciated. The authors would also like to express their gratitude to Mr. Trond Auestad for his contributions during the experimental work.

References

[1] Qi R, Langdon GS, Cloete TJ, Yuen CK. Behaviour of a blast-driven ball bearing embedded in rear detonated cylindrical explosive. Int J Impact Eng 2020;146:103698.
[2] Leppanen J. Concrete structures subjected to fragment impacts, dynamic behaviour and material modelling (Ph.D. thesis), Department of Structural Engineering and Mechanics, Concrete Structures, Chalmers University of Technology; 2004.
[3] Nystrøm U, Gylltoft K. Numerical studies of the combined effects of blast and fragment loading. Int J Impact Eng 2009;36:995—1005.
[4] Grisaro HY, Dancygier AN. Characteristics of combined blast and fragments loading. Int J Impact Eng 2018;116:51—64.
[5] Marchand KA, Vargas MM, Nixon JD. The synergistic effects of combined blast and fragment loadings. Tech. rep, San Antonio Texas; 1992.
[6] Hyde DW, Station UAEWE, of Engineers USAC. User's guide for microcomputer programs conwep and funpro, applications of tm 5-855-1, "fundamentals of protective design for conventional weapons". Instruction report, U.S. Army Engineer Waterways Experiment Station; 1988, URL https://books.google.no/books?id=xhHxHAAACAAJ.
[7] Kong X, Wu W, Li J, Chen P, Liu F. Experimental and numerical investigations on a multi-layer protective structure under the synergic effect of blast and fragment loadings. Int J Impact Eng 2014;65:146–62.
[8] Leppänen J. Experiments and numerical analyses of blast and fragment impacts on concrete. Int J Impact Eng 2005;31(7):843–60.
[9] Grisaro HY, Dancygier AN. Dynamic response of RC elements subjected to combined loading of blast and fragments. J Struct Eng 2020;147:04020315.
[10] Grisaro HY. Effect of combined blast and fragmentation load on the dynamic response of reinforced concrete structures. Eng Struct 2021;248.
[11] Linz PD, Fan SC, Lee CK. Modeling of combined impact and blast loading on reinforced concrete slabs. Lat Am J Solids Struct 2016;13:2266–82.
[12] Linz PD, Fung TC, Lee CK, Riedel W. Response mechanisms of reinforced concrete panels to the combined effect of close-in blast and fragments: An integrated experimental and numerical analysis. Int J Prot Struct 2020.
[13] Yuan Y, Tan P. Deformation and failure of rectangular plates subjected to impulsive loadings. Int J Impact Eng 2013;59:46–59.
[14] Li L, Zhang Q-C, Zhang R, Wang X, Zhao Z-Y, He S-Y, Han B, Lu TJ. A laboratory experimental technique for simulating combined blast and impact loading. Int J Impact Eng 2019;134:103382.
[15] Li W, Wang P, Feng G-P, Lu Y-G, Yue J-Z, Li H-M. The deformation and failure mechanism of cylindrical shell and square plate with pre-formed holes under blast loading. Defence Technology 2020;17(4):1143–59.
[16] Aune V, Valsamos G, Casadei F, Langseth M, Børvik T. On the dynamic response of blast-loaded steel plates with and without pre-formed holes. Int J Impact Eng 2017;108:27—46.
[17] Li Y, Wu W, Zhu H, Wua Z, Dub Z. The influence of different pre-formed holes on the dynamic response of square plates under air-blast loading. Eng Fail Anal 2017;78:122—133.
[18] Rakvåg K, Underwood N, Schleyer G, Børvik T, Hopperstad O. Transient pressure loading of clamped metallic plates with pre-formed holes. Int J Impact Eng 2012;53:44—55.
[19] Zhang C, Tan P, Yuan Y. Confined blast loading of steel plates with and without pre-formed holes. Int J Impact Eng 2022;163:104183.
[20] Granum H, Aune V, Børvik T, Hopperstad OS. Effect of heat-treatment on the structural response of blast-loaded aluminium plates with pre-cut slits. Int J Impact Eng 2019;132:103306.
[21] Cai S, Liu J, Zhang P, Li C, Cheng Y, Chen C. Experimental study on failure mechanisms of sandwich panels with multi-layered aluminum foam/UHMWPE laminate core under combined blast and fragments loading. Thin-Walled Struct 2021;159:107227. http://dx.doi.org/10.1016/j.tws.2020.107227.
[22] Li J, Huang C, Ma T, Xiancong H, Li W, Liu M. Numerical investigation of composite laminate subjected to combined loadings with blast and fragments. Compos Struct 2019;214. http://dx.doi.org/10.1016/j.compstruct.2019.02.019.

[23] Holmen JK, Hopperstad OS, Børvik T. Influence of yield-surface shape in simulation of ballistic impact. Int J Impact Eng 2017;108:136–46.
[24] Dey S, Børvik T, Hopperstad OS, Leinum JR, Langseth M. The effect of target strength on the perforation of steel plates using three different projectile nose shapes. Int J Impact Eng 2004;30:1005–38.
[25] Spranghers K, Vasilakos I, Lecompte D, Sol H, Vantomme J. Full-field deformation measurements of aluminum plates under free air blast loading. Exp Mech 2012;52:1371–84.
[26] Aune V, Fagerholt E, Hauge K, Langseth M, Børvik T. Experimental study on the response of thin aluminium and steel plates subjected to airblast loading. Int J Impact Eng 2012;90:106—121.
[27] Elveli BS, Iddberg MB, Børvik T, Aune V. On the strength-ductility trade-off in thin blast-loaded steel plates with and without initial defects - An experimental study. Thin-Walled Struct 2022;171:108787.
[28] SSAB. Docol automotive steels. 2020, [Online; accessed 23-May-2022] https://www.ssab.com/products/brands/docol.
[29] Gruben G, Langseth M, Fagerholt E, Hopperstad O. Low-velocity impact on high-strength steel sheets: An experimental and numerical study. Int J Impact Eng 2016;88:153—171.
[30] Børvik T, Langseth M, Hopperstad O, Malo K. Ballistic penetration of steel plates. Int J Impact Eng 1999;22(9):855–86.
[31] Fagerholt E. [Online; accessed 23-May-2022] https://www.ntnu.edu/kt/ecorr, 2008.
[32] Aune V, Fagerholt E, Langseth M, Børvik T. A shock tube facility to generate blast loading on structures. Int J Prot Struct 2016;7:340—366.
[33] Tasissa AF, Hautefeuille M, Fitek JH, Radovitzky RA. On the formation of friedlander waves in a compressed-gas-driven shock tube. Proc R Soc A: Math, Phys Eng Sci 2016;472:20150611.
[34] Aune V, Valsamos G, Casadei F, Langseth M, Børvik T. Fluid-structure interaction effects during the dynamic response of clamped thin steel plates exposed to blast loading. Int J Mech Sci 2021;195:106263. http://dx.doi.org/10.1016/j.ijmecsci.2020.106263.
[35] Abrahamsen B, Alsos H, Aune V, Fagerholt E, Faltinsen O, Hellan O. Hydroplastic response of a square plate due to impact on calm water. Phys Fluids 2020;32. http://dx.doi.org/10.1063/5.0013858.1.
[36] US Army Corps of Engineers (USACE). Structures to resist the effects of accidental explosions. Washington DC: UFC 3-340-02. Supersedes TM5-1300, dated November 1990. US Department of Defense; 2008.
[37] Børvik T, Hopperstad OS, Berstad T, Langseth M. A computational model of viscoplasticity and ductile damage for impact and penetration. Eur J Mech A/Solids 2001;20:685—712.
[38] Børvik T, Hopperstad O, Berstad T, Langseth M. Perforation of 12mm thick steel plates by 20mm diameter projectiles with flat, hemispherical and conical noses - Part II: Numerical simulations. Int J Impact Eng 2002;27:37–64.
[39] Cockcroft MG, Latham DJ. Ductility and workability of metals. J. Inst Met 1968;96:33—39.
[40] Erhart T. Review of solid element formulations in LS-DYNA. 2011, [Online; accessed 23-May-2022] https://www.dynamore.de/en/downloads/papers/forum11/entwicklerforum-2011/erhart.pdf/view.
[41] Holmen JK, Johnsen J, Hopperstad O, Børvik T. Influence of fragmentation on the capacity of aluminum alloy plates subjected to ballistic impact. Eur J Mech A Solids 2016;55:221–33.
[42] Holmen JK, Børvik T, Hopperstad O. Experiments and simulations of empty and sand-filled aluminum alloy panels subjected to ballistic impact. Eng Struct 2017;130:216–28.